

Additive manufacturing of functionally graded inconel 718

Effect of heat treatment and building orientation on microstructure and fatigue behaviour

Ghorbanpour, Saeede; Deshmukh, Kaustubh; Sahu, Saswat; Riemslag, Ton; Reinton, Elise; Borisov, Evgenii; Jiang, Quanxin; Sanchez, María Terol; Knezevic, Marko; Popovich, Vera

DOI

[10.1016/j.jmatprotec.2022.117573](https://doi.org/10.1016/j.jmatprotec.2022.117573)

Publication date

2022

Document Version

Final published version

Published in

Journal of Materials Processing Technology

Citation (APA)

Ghorbanpour, S., Deshmukh, K., Sahu, S., Riemslag, T., Reinton, E., Borisov, E., Jiang, Q., Sanchez, M. T., Knezevic, M., Popovich, V., & More Authors (2022). Additive manufacturing of functionally graded inconel 718: Effect of heat treatment and building orientation on microstructure and fatigue behaviour. *Journal of Materials Processing Technology*, 306, Article 117573. <https://doi.org/10.1016/j.jmatprotec.2022.117573>

Important note

To cite this publication, please use the final published version (if applicable).
Please check the document version above.

Copyright

Other than for strictly personal use, it is not permitted to download, forward or distribute the text or part of it, without the consent of the author(s) and/or copyright holder(s), unless the work is under an open content license such as Creative Commons.

Takedown policy

Please contact us and provide details if you believe this document breaches copyrights.
We will remove access to the work immediately and investigate your claim.



Additive manufacturing of functionally graded inconel 718: Effect of heat treatment and building orientation on microstructure and fatigue behaviour

Saeede Ghorbanpour^{a,*}, Kaustubh Deshmukh^a, Saswat Sahu^a, Ton Riemslag^a, Elise Reinton^a, Evgenii Borisov^b, Anatolii Popovich^b, Virginia Bertolo^a, Quanxin Jiang^a, María Terol Sanchez^a, Marko Knezevic^c, Vera Popovich^{a,b,**}

^a Department of Materials Science and Engineering, Delft University of Technology, The Netherlands

^b Peter the Great Saint-Petersburg Polytechnic University, Saint Petersburg, Russia

^c Department of Mechanical Engineering, University of New Hampshire, Durham, NH 03824, USA

ARTICLE INFO

Associate Editor: Jingjing Li

Keywords:

Laser powder bed fusion
Inconel 718
Fatigue crack growth behaviour
Heat treatment
Functional grading

ABSTRACT

This paper addresses the effect of the post-process heat treatments on the microstructure and fatigue crack growth behaviour of the functionally graded (FG) laser powder bed fusion (L-PBF) Inconel 718 (IN718) superalloy. Sets of samples were additively manufactured (AM) altering the process parameters, namely the laser power, the laser scanning speed, layer thickness, hatch distance, and beam distribution function, resulting in distinctly different microstructures. Two categories of samples underwent heat treatment (HT) and hot isostatic pressing followed by HT (HIP+HT), while one category was kept in the as-processed (AP) condition to reveal the effects of the post-treatments. Additionally, to study the effect of microstructural anisotropy, samples were printed in horizontal (H) and vertical (V) building directions. To better understand the behaviour of the FG materials, non-graded (NG) L-PBF samples and wrought material were investigated as references. Significant variations in terms of porosity, grain size and elongation, crystallographic texture, and content of the strengthening precipitates or detrimental phases were found in different AM groups. The fatigue behaviour of the NG and FG materials was also studied by conducting three-point bending tests. Findings in terms of the role of different microstructures on the fatigue-crack initiation and fatigue crack growth rate are presented and discussed for all samples. The study demonstrated that heat treatments can enhance the damage tolerance of L-PBF IN718 to the level of wrought material. Interestingly, the effect of the roughness induced crack closure was found to be a function of build orientation, especially in the low stress ratio regime.

1. Introduction

Laser powder bed fusion (L-PBF) is an additive manufacturing (AM) process which allows for producing complex geometries using computer aided design (CAD) models (Popovich et al., 2017a). Despite many advantages of the AM methods, including the capability of producing functionally graded (FG) parts and a significantly lower buy-to-fly ratio (BTF) compared with the conventional manufacturing procedures, tensile residual stresses (Hönnige et al., 2021), detrimental phases (Knezevic et al., 2021) and defects (Wang and Chou, 2019) might be introduced into the additive manufactured parts which affect the

mechanical properties. Post-processing heat treatments can then be employed to reduce these detrimental effects and enhance the properties.

Inconel 718 (IN718) is a precipitate hardened nickel-based superalloy. The main strengthening precipitates of the Al γ matrix (Gribbin et al., 2019) are coherent ordered (Oblak et al., 1974) γ' (Ni_3Al) with an L1_2 lattice structure and γ'' (Ni_3Nb) with a DO_{22} structure (Hosseini and Popovich, 2019). γ' precipitates are spherical shaped with diameters ranging between 10 and 40 nm, while γ'' precipitates are disk shaped with diameters of 20–30 nm and thickness of 5–6 nm (Ghorbanpour et al., 2017). In addition to the strengthening precipitates, other phases

* Corresponding author.

** Corresponding author at: Department of Materials Science and Engineering, Delft University of Technology, the Netherlands.

E-mail addresses: S.Ghorbanpour@tudelft.nl (S. Ghorbanpour), v.popovich@tudelft.nl (V. Popovich).

<https://doi.org/10.1016/j.jmatprotec.2022.117573>

Received 6 November 2021; Received in revised form 23 March 2022; Accepted 27 March 2022

Available online 29 April 2022

0924-0136/© 2022 The Author(s). Published by Elsevier B.V. This is an open access article under the CC BY license (<http://creativecommons.org/licenses/by/4.0/>).

such as hexagonal Laves $(\text{Ni,Fe,Cr})_2(\text{Nb,Mo,Ti})$, orthorhombic δ (Ni_3Nb), and MC carbides could be present in the alloy (Hosseini and Popovich, 2019). Hard and brittle irregular shape micron-sized Laves phase forms at the end of the solidification process due to the micro-segregation of the alloying elements (Popovich et al., 2017b). Due to the low diffusion rate of Nb in the γ matrix, the Laves phases tend to form on the grain boundaries and in interdendritic regions (Nezhadfar et al., 2020). The intermetallic Laves phase is known to have detrimental effects on mechanical properties, including fatigue properties since they can promote the crack initiation and propagation at high stress amplitudes (Sui et al., 2017). The δ phase, in the form of 1–8 μm needle-like incoherent precipitates (Burke and Miller, 1991), is known to be detrimental to mechanical properties except the high temperature creep rupture strength (Sanchez et al., 2021). Brittle MC carbides with rough morphologies are also known to form at the grain boundaries, like the δ phase (Mostafa et al., 2017).

Post-process heat treatments are common procedures to improve the properties of AM parts by minimizing the effects of the non-equilibrium phases and thermal residual stresses (Chlebus et al., 2015). Solutionizing at temperatures around 1000 $^\circ\text{C}$ followed by aging is a well-adapted heat treatment used for Inconel superalloys. Solutionizing at 980 $^\circ\text{C}$ and double aging (DA) results in precipitation of the δ phase at grain boundaries (Wang et al., 2012) in addition to preserving some of the Laves phases due to the inefficiency of the temperature to dissolve all those phases (Zhang et al., 2015). Applying the AMS 5663 (5663, 1965) heat treatment to the L-PBF material increases the δ volume fraction to about 6% (Ferreri et al., 2020). It is also reported that heat treatment results in the disappearance of the dendritic structures formed during the AM process (Moussaoui et al., 2018). Similarly, solution treatment at a higher temperature of 1050 $^\circ\text{C}$ followed by the double aging procedure results in the dispersion of the δ phase in grain boundaries and vanishing the dendritic structures (Feng et al., 2017).

The presence of porosity is one of the obstacles deteriorating mechanical properties, particularly in cyclic loading conditions. The hot isostatic pressing (HIP) procedure is a post-processing treatment used to decrease internal pores. By subjecting the specimens to high pressure at high temperature as done in HIP treatment it was shown possible to significantly reduce internal porosity and the size of surface porosity associated with AM process (Karami et al., 2020). HIP treatment of the L-PBF IN718, at a temperature and pressure of above 1150 $^\circ\text{C}$ and 100–150 MPa respectively, with a holding time of 2 h, was found to reduce the volume fraction of the porosity from 0.3% to 0.07% (Popovich et al., 2017b). It is worth noting that, due to the entrapped argon gas in the AM parts, the existence of some porosity is inevitable (Tillmann et al., 2017).

In several studies the effect of various post-processing treatments on the improvement of mechanical properties, including hardness, tensile strengths, room temperature and high temperature ductility, high cycle (HCF) and low cyclic fatigue behaviour were investigated. Studying different post-processing treatments on the SLM IN718 revealed that HIP followed by homogenization and double aging results in superior tensile properties due to dissolution of Laves and δ phase, pores closure, and size and density increase of carbides (Popovich et al., 2017b). Yield strength and ultimate tensile strength of an SLM IN718 increased from 889 to 907 MPa, and 1137–1148 MPa to 1102–1161 MPa and 1280–1358 MPa respectively, when a solution and age hardening post treatment was applied (Wang et al., 2012). Furthermore, an increase of about 30% was reported in the microhardness of the SLM material after heat treatment. The HCF behaviour of double-aged AM samples was reported to be superior to the heat treated wrought samples at low stress amplitudes (lower than 630 MPa) due to the presence of unbroken Laves phases, which hindered the crack propagation (Sui et al., 2017). The high temperature HCF behaviour of heat treated AM IN718 was found to be similar to the wrought samples and outperform the HIP+HT specimens. This behaviour is attributed to the domination of coarse grains in the structure and the high content of incoherent annealing twins in

HIP+HT material which affected the cyclic life more than the presence of porosity and δ phase (Gribbin et al., 2019). The room temperature LCF lives of the AM HT samples at strain amplitudes lower than 0.8% were reported to be higher than the wrought-HT materials, while it was the opposite for the higher strain amplitudes, and it was rationalized by the effect of the AM induced porosity (Gribbin et al., 2016b). Similar to the weaker HCF properties of the HIP+HT samples compared with the AM-HT and Wrought-HT materials (Gribbin et al., 2019), the LCF behaviour of HIP+HT samples was affected by the incoherent annealing twins, and their lives were shorter than the other counterparts (Gribbin et al., 2016b).

Moreover, the effect of post-processing on the crystallographic texture of the nickel-based superalloys has been explored. One hour annealing at 1080 $^\circ\text{C}$ or two hours solution annealing at 1150 $^\circ\text{C}$ of the L-PBF Inconel 625 were observed to eliminate the texture, reduce the low angle grain boundaries (LAGBs), and increase the high angle grain boundaries and twin angle boundaries (Marchese et al., 2020). It was also reported that the solution treatment further weakens the $\langle 100 \rangle$ texture and spreads it towards the $\langle 110 \rangle$, and HIP results in a random texture (Kreitzberg et al., 2017), (Kouraytem et al., 2021). All these microstructural aspects are yet to be investigated in details with respect to their effects on fatigue crack growth behaviour.

Despite the extensive research on the influence of post-process heat treatments on various mechanical properties, the effects of the post treatment and microstructural anisotropy such as grain size, grain orientation, and texture on the fatigue crack growth rate (FCGR) of the functionally graded IN718 has not been investigated yet. In this study, we focused on the influence of the HT (AMS 5383 (5383, 1966)) and HIP+HT (AMS 5664E (5664E, 1965)) procedures and subsequent different microstructural features and textures on the threshold for fatigue-crack initiation (ΔK_{th}) and FCGR of the L-PBF IN718. A variety of specimens with different notch position with respect to the building orientation were fabricated. In addition to the different laser powers used in the non-graded materials, two categories of functionally graded materials (FGM) were produced and post processed. The results of this study were compared to the properties which were found from examining the as-processed (AP) L-PBF materials and wrought samples.

2. Materials and experiments

2.1. IN718 samples manufacturing and post treatment

IN718 alloy powder made by gas atomization, with the chemical composition provided in Table 1 and the distribution of $d_{10} = 20 \mu\text{m}$ and $d_{90} = 64 \mu\text{m}$, was used for L-PBF manufacturing. The IN718 fatigue crack growth rate test specimens were fabricated by an SLM 280^{HL} unit using a laser wavelength of 1070 nm. To accommodate a variety of microstructures, different manufacturing parameters including laser power (P), laser scanning speed (V), layer thickness (t), and hatch distance (h) were selected in a way that their combined effect, which is defined as the volume energy density (VED), E_v , remained around the constant value of 59.5 J/mm^3 . In addition to the mentioned parameters, the effect of the Gaussian and flat top beam distribution with different beam diameters were explored. The layer thickness of the low energy samples was set to be 50 μm while it was 100 μm for the high energy specimens. Table 2 gives a summary of the processing parameters used for manufacturing the samples for the current study. Fig. 1 shows the schematics of the non-graded (NG) and functionally graded (FG) samples manufactured for this study. The same parameters which are explained for the non-graded samples are used for the lower laser power and higher laser power parts of the FG samples. For the FG samples printed in the H direction, as shown in Fig. 1(d), the lower half of the sample was fabricated in a low-energy mode, then from a certain layer the mode was changed to a high-energy one. For the FG-V samples, half of the sample (the left part in the figure) was made according to the low-energy regime, and the other half (the right side in the figure) was built according to the high-energy

Table 1

Alloy IN718 elemental composition measured by scanning electron microscopy electron dispersive spectroscopy (SEM EDS).

| Element | Ni | Cr | Fe | Nb | Mo | Ti | Al | Mn | Co |
|---------|-------|-------|-------|-----|-----|------|------|------|-----|
| wt% | 51.45 | 19.38 | 18.49 | 5.3 | 3.4 | 1.04 | 0.72 | 0.12 | 0.1 |

Table 2

L-PBF manufacturing parameters.

| Sample orientation | Laser power [W] | Laser scanning speed [mm/s] | Layer thickness [mm] | Hatch distance [mm] | Beam distribution function | Beam diameter [μm] |
|--------------------|-----------------|-----------------------------|----------------------|---------------------|----------------------------|---------------------------------|
| H | 250 | 700 | 0.05 | 0.12 | Gaussian | 80 |
| H | 950 | 320 | 0.1 | 0.5 | Flat top | 100 |
| V | 950 | 320 | 0.1 | 0.5 | Flat top | 100 |

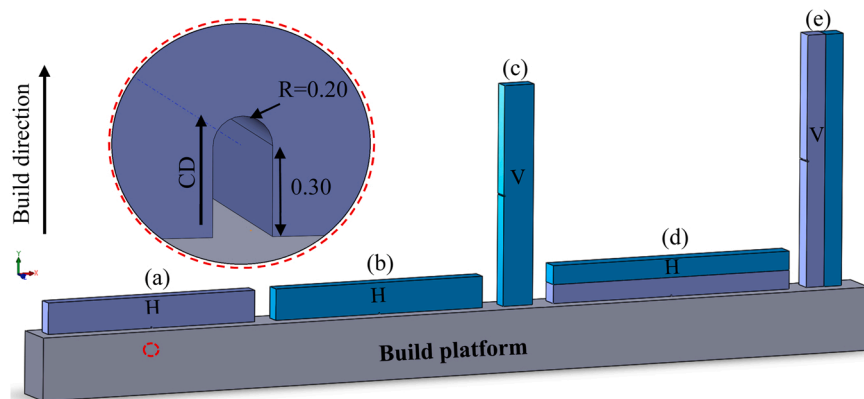


Fig. 1. Orientation of the samples with respect to the build (BD) and crack direction (CD) for non-graded: (a) 250 W-H, (b) 950 W-H, (c) 950 W-V, as well as functionally graded specimens: (d) horizontal (H), and (e) vertical (V). The notch dimensions are provided in mm in the insert. Purple colour shows the parts manufactured using 250 W parameter set and green colour depicts the parts manufactured using 950 W set of parameters. (For interpretation of the references to colour in this figure legend, the reader is referred to the web version of this article.)

regime. Contouring was performed separately along the border of the low-energy and high-energy zones. In the interface zone, the boundaries of the axes of the contours were spaced at a distance of about $80 \mu\text{m}$. Since the high-energy mode had a larger laser beam diameter than the low-energy mode, a certain volume of material processed by the low-energy mode was re-melted.

To further investigate the effect of the microstructural anisotropy on the FCGR, two categories of samples were designed and manufactured considering the depositing build direction (BD) and the initial notch direction (the same as the crack direction (CD) during the tests). In all specimens, the crack direction was located on the vertical symmetry axis of the samples. As shown in Fig. 1, the directional samples studied in this research were horizontal (H) with parallel BD and CD and vertical (V) with perpendicular BD and CD. Finally, specimens were built in the of NG form with laser specifications remaining the same during sample fabrication, and) FG form with transitions of the laser parameters during the manufacturing process. All samples were designed and made to satisfy the conditions provided in ASTM E399 (Maciejewski et al., 2013). NG samples had the size of 70 mm length, 10 mm height, and 5 mm width. The dimensions were slightly larger for the FG samples as 80 mm length, 12 mm height, and 6 mm width. The notch with a total depth of 0.5 mm and a radius of 0.2 mm was made by the electrical discharge machining (EDM) in NG and FG samples.

Manufactured samples were divided into three categories for post-processing purposes. The first group was explored in the as-processed (AP) condition. The detailed characterization and experimental results of this category are reported in our previous study (Ghorbanpour et al., 2021). The second category was heat treated according to AMS 5383 (5383, 1966), which consists of a homogenisation step at $1080 \text{ }^\circ\text{C}$ for 1.5 h followed by the procedure described in AMS 5663 (5663, 1965), which includes a solutionizing at $980 \text{ }^\circ\text{C}$ for 1 h followed by a double-aging procedure at $720 \text{ }^\circ\text{C}$ and $620 \text{ }^\circ\text{C}$ each step for 8 h. In this study, the samples of this category are referred to as the heat treated (HT) ones. The other group of the AM material underwent the hot

isostatic pressing (HIP) procedure, followed by an AMS 5664E (5664E, 1965) heat treatment. The HIP procedure was done at $1180 \text{ }^\circ\text{C}$ and a pressure of 150 MPa for 3 h. The heat treatment contained a homogenisation at $1065 \text{ }^\circ\text{C}$ for 1 h, followed by a double aging process at $760 \text{ }^\circ\text{C}$ for 10 h, and at $650 \text{ }^\circ\text{C}$ for 8 h. These samples are referred to as HIP+HT hereon. In addition to the L-PBF specimens, a group of wrought material samples was made and heat treated based on AMS 5663. Table 3 gives a summary of the post treatment procedures of the L-PBF and wrought samples used in this study.

2.2. Microstructural characterization

Grain morphology, the presence and distribution of the precipitates and carbides, and different structures resulted from various manufacturing parameters and post-treatments were investigated utilizing the optical microscopy and scanning electron microscopy (SEM) techniques. The samples were prepared for the optical microscopy and SEM analyses by grinding, polishing, and etching. The final step of the polishing was done using a $1 \mu\text{m}$ silica suspension. The Glyceregia etchant solution, which consists of 15 ml HCl, 10 ml Glycerol, and 5 ml HNO_3 , was used to etch the surfaces for about 3 s. Optical microscopy was done using a Leica DMLM optical microscope with analysis 5.0 by Olympus soft Imaging Solutions GmbH, and a Keyence VHX-5000 device. A JEOL JSM IT-100 SEM equipped with JEOL InTouchScope software was used for exploring the surfaces prior to the tests along with the fracture surface analyses.

X-ray diffraction (XRD) measurements of the AP, HT, and HIP+HT L-PBF materials were carried out using a Bruker D8 advanced diffractometer with a graphite monochromator. The unit was equipped with a $\text{Co K}\alpha$ X-ray beam generator and a Vantec position sensitive detector. The measurements were done using a wavelength of 1.78897 \AA and a scanning step size of 0.035 degrees in a 2θ scale between 20 and 140 degrees. To further analyse the XRD data, Bruker software Diffrac was used.

Table 3
A summary of the post-processing heat treatments.

| Group | Post-process heat treatment | Temperature [°C] | Holding time [h] | Cooling specification | |
|--------------|-----------------------------|------------------|------------------|-----------------------|----------------------|
| L-PBF | AP | – | – | – | |
| | HT (AMS 5383) | Homogenisation | 1080 | 1.5 | Air cooling (AC) |
| | | Solutionizing | 980 | 1.5 | AC |
| | | Double-aging | 720 | 8 | Furnace cooling (FC) |
| | HIP+HT (AMS 5664E) | 620 | 8 | AC | |
| | | HIP (at 150 MPa) | 1180 | 3 | FC |
| | | Homogenisation | 1065 | 1 | AC |
| | | Double-aging | 760 | 10 | FC |
| | Wrought with HT (AMS 5663) | 650 | 8 | AC | |
| | | Solutionizing | 980 | 1 | AC |
| Double-aging | | 720 | 8 | FC | |
| 620 | | 8 | AC | | |

To understand the impact of the post-processing procedures on the localized plastic deformation resistance, Vickers hardness tests were performed. A Struers DuraScan G5 testing machine was used to perform the tests at a load of 1000 gf (HV1) and the holding time of 10 s. The NG samples' hardness measurements were replicated on ten random spots of the surface to ensure the repeatability and precision of the tests. For the FG samples, however, the measurements were done in lines along the width of the samples to explore the possible influence of the microstructural gradient in the interface zone. In addition, the measurements were carried out on multiple locations to investigate the effect of the build direction and thermal cycles on the hardness.

Furthermore, the porosity content and distribution in the L-PBF materials in AP, HT, and HIP+HT conditions were measured. The Keyence VHX-5000 microscope was used for the porosity analysis. The measured surface areas were 2000 μm * 2000 μm and for accuracy and reproducibility purposes, measurements of each category was repeated at least three times on different areas. Due to the resolution limits of the device pores with diameters larger than 1 μm were detected.

Grain structures and crystallographic textures of all categories of NG materials before the fatigue tests were acquired using the electron backscattered diffraction (EBSD) technique. Samples were prepared similar to the preparation procedure explained for the optical microscopy and SEM, with an additional polishing step with 0.25 μm colloidal silica suspension. The etching was not necessary, instead, an ultrasonic bath cleaning with isopropanol was added as the final step. An SEM Mira 3 Tescan equipped with channel 5- HKL software, with an accelerating voltage of 20 kV, was used to collect the EBSD data. Moreover, the same technique was used to study the crack growth path of the FG samples. Depending on the optical microscopy and SEM micrographs, the step size was chosen differently between 0.8 μm and 1.7 μm . The collected EBSD data were post processed using TSL-OIM analysis software version 8. Prior to the tests, for each category of materials, multiple areas were imaged to have a reasonable number of grains detected. Based on the grain size estimates, the EBSD imaging step size varied between 0.5 μm and 1.7 μm . The minimum average confidence index (CI) of all measurements was 0.35. In all measurements, at least 96.6% of the collected data, which varied between 1393644 and 6293324 points, were indexed. The data was cleaned up using the Neighbor CI Correlation (NCIC) clean-up procedure with the "minimum confidence index" parameter set to be 0.3. A generalized spherical harmonic expansion smoothing with series rank $L=16$, a Gaussian half-width of 5 degrees, and triclinic symmetry were used to plot the stereographic pole figures. Multiple EBSD imaging along the crack of the FG specimens and the wrought sample was done to cover a good length of the crack path. To avoid introducing artefacts on the crack path, clean-up procedures were not used.

2.3. Fatigue testing and modelling

To study the fatigue crack growth behaviour of the NG and FG parts, three-point bending fatigue tests with stress intensity factor (SIF)

solutions and test configurations in accordance with ASTM E399 (Maciejewski et al., 2013) were conducted. A hydraulic MTS machine, with a capacity of 25 kN, with the MTS MultiPurpose TestWare and Flextest electronic unit, was used for testing purposes. A direct current potential drop (DCPD) equipment with a measurement resolution of 0.5 mm was used to ascertain the correlation between the visually measured crack length and the output voltage. It should be noted that the visual crack calibration and propagation measurement were done using two Limes digital image correlation (DIC) 5-megapixel cameras.

The NG samples were tested under constant K_{max} condition, which allowed to measure the threshold stress intensity factor range (ΔK_{th}). The frequency of the constant K_{max} tests was 30 Hz. The stress ratio (R), which is defined by Eq. 1, initially was set to be 0.1 in all constant K_{max} tests and was increased to values around 0.6–0.7 by the end of the tests. To obtain a sufficient ΔK which allowed for the crack growth, the K_{max} value was calculated from Eq. 2 and was kept constant during the tests. The value of K_{min} was calculated by the formula given in Eq. 3.

$$R = \frac{K_{\text{min}}}{K_{\text{max}}} \quad (1)$$

$$K_{\text{max}} = \frac{\Delta K}{1 - R} \quad (2)$$

$$K_{\text{min}} = K_0 e^{(C(a-a_0))} \quad (3)$$

Where K_0 is the initial K_{min} value, C is the gradient of the SIF and was set to be -0.4 1/mm, a is the instantaneous crack length measured by DCPD, which was validated by optical and DIC observations, and a_0 is the initial crack length measured by DIC. The value of K_{min} was ramped up during the test to maintain the K_{max} -constant condition. The adjustment of K_{min} was stopped when the crack growth was less than 0.1 mm during 100,000 cycles which is equal to a crack growth rate of 10^{-6} mm/cycle or lower. The ΔK reading of this stage is regarded as ΔK_{th} .

The other type of experiment which was done on the NG samples was the constant load amplitude tests. The objective of these tests was to formulate the crack growth rate as a function of the SIF range (ΔK). The experimental procedure was in accordance with ASTM-E647 (E647) and the test frequency was set to be 50 Hz. The curves obtained from the constant load amplitude tests in the Paris regime were fit linearly to calculate the Paris constant and Paris exponent values.

To explore the effect of the microstructure of the functionally graded samples on the fatigue crack growth rate, three-point bending tests in the constant SIF range were carried out. It is known that for a given ΔK , and a specific microstructure, the FCGR remains about a constant value. Therefore, the effect of the functionally graded structure on the FCGR should be exposed if K remains constant. The standard K solutions to determine the load levels, which are described based on the crack length and sample width, are developed for homogeneous materials and thus are not applicable for the functionally graded components. Therefore, to have accurate, customized K solutions for the FGM IN718 parts, an elastic FEA model within ABAQUS was developed. The functionally

graded samples were simulated as two main halves of the NG materials, which were joint by the interface layer. Materials are modelled with linear elasticity. For the main halves, Young's moduli of the corresponding NG samples, which were measured from the compliance of the fatigue tests and are provided in Table 4, were used. The 1 mm interface was divided into five geometrically homologous layers, each of which had its E adjusted linearly. The Poisson's ratio of all parts was set to be 0.3. Based on symmetry, a half-span of the specimen is modelled under a 2D plane strain condition, where crack is modelled at the symmetry plane. At the symmetry plane, the displacement along X axis is constrained at the non-cracked edge, while free boundary condition is applied to the crack. The applied load is modelled with a 5 kN point load along the negative Y direction at the top edge. The support is modelled as a point pinned constraint at the bottom edge. The model which was used for all three post-treatment categories had the same element types and element numbers. Mesh elements near the crack tip were 0.02 mm. The mesh element size was increased to 0.5 mm in the areas which were not highly influenced by the crack. The types of the elements in the model were CPE6M (6- node modified quadratic plane strain element with hourglass control) and CPE8R (8-node biquadratic plane strain element with reduced integration) and the mesh element numbers were 185 and 4456, respectively. Fig. 2 demonstrates the model which was used in this study. The output of the model was the J-integral value (J), which was employed to calculate the customized K solutions using Eq. 4.

$$K = \sqrt{J \times \frac{E}{1 - \nu^2}} \quad (4)$$

Where E is Young's modulus at the crack tip, and ν is the Poisson's ratio.

3. Results and discussion

3.1. Microstructural analyses

To explore the effect of the post-treatment procedures on the interface zone of the FG samples, optical microscopy images were taken. The optical micrographs over the longitudinal cross sections of the FG samples of AP and post-treated categories are provided in Fig. 3. As can be seen in Fig. 3a and b, the melt pools which were introduced by AM are clearly visible with different characteristics in areas of 250 W and 950 W laser powers. The transition from the 250 W region to the 950 W zone was observed to be smooth in the horizontal sample since the laser parameters remained the same in any individual deposited layers. However, the interface area of the AP vertical sample was distinguishable with finer melt pools in the centre and deeper melt pools on the edges, key-hole induced porosities, and unmelted particles, which are the artefacts caused by the change of the laser parameters in the deposition. In both categories of the AP condition, grains were elongated in the building direction. After HT, the grains of both build orientations remained elongated in the BD, which indicates that the homogenisation temperature was not high enough to induce full grain recrystallization. However, the patterns of the deposition layers and melt pools

Table 4

Young's moduli measured on the wrought, AP, HT, and HIP+HT materials using the three-point bending tests.

| Processing condition | Sample category | Young's modulus [GPa] |
|----------------------|-----------------|-----------------------|
| Wrought | – | 181 ± 5 |
| L-PBF- AP | 250 W | 186 ± 15 |
| | 950 W- H | 136 ± 10 |
| | 950 W- V | 139 ± 36 |
| L-PBF- HT | 250 W | 159 ± 21 |
| | 950 W- H | 130 ± 9 |
| | 950 W- V | 132 ± 8 |
| L-PBF- HIP+HT | 250 W | 188 ± 22 |
| | 950 W- H | 170 ± 26 |
| | 950 W- V | 160 ± 21 |

boundaries were faint as compared to AP condition. As an influence of the HT, the boundaries of the interfaces were not distinct despite what was observed in the AP samples. Nonetheless, the defects and porosities were still present, and similar to the AP samples, were more pronounced in the V specimens. The HIP+HT procedure, however, resulted in a completely different microstructure, as can be seen in Fig. 3e and f. The melt pool tracks of the deposited layers, and columnar grains were not detected. Similar to the HT specimens, the transitions at the interface zone for both sample orientations were smooth. The population of the captured defects was significantly lower compared with the other two categories.

To further study the microstructure, SEM images of the NG samples in the AP and post-treated conditions were taken. Fig. 4 shows the SEM micrographs of the AP materials along with the samples' build direction. Elongated grains, extended in the build direction, and the melt pool patterns were observed in all SEM images. The major axes of the grains in both 250 W and 950 W laser power groups were found to exceed the deposited layer thickness of those categories, which were 50 μm and 100 μm , respectively. This phenomenon implies the melting of those previously solidified layers and a clear pattern of the epitaxial grain growth through the deposited layers (Popovich et al., 2017a).

The SEM micrographs of the HT IN718 specimens are provided in Fig. 5. The micrographs show the growth of the dendritic structure of the γ matrix along the BD. The other feature which was observed in the HT materials' micrographs is the presence of the rod-like and globular δ precipitates, which were not found in the AP material. The volume fraction of the δ phase in the HT L-PBF IN718 was reported to be 5.9 ± 0.4 (Ferreri et al., 2020). It was reported that the δ phase interacts differently with the crack tip depending on its relative direction, i.e. if they are parallel or perpendicular to the crack growth orientation. However, generally the presence of the δ phase decreases the crack growth rate since the deformation and fracture of the δ phase consumes energy (Iyer et al., 2017). In previous studies (Ponnelle et al., 2001) it was reported that delta phase interacts differently with the crack tip depending on its relative direction, i.e. if they are parallel or perpendicular to the crack growth orientation. When δ -phases were oriented perpendicular compared to the parallel to the loading direction, the crack growth rates were approximately ten times faster. Furthermore, crack growth occurred preferably in the interface between the γ -matrix and the δ -phase. In general, the presence of the δ phase decreases the crack growth rate since the deformation and fracture of the δ phase consumes energy. A moderate volume fraction of the δ phase was also found to improve the mechanical properties, e.g., enhancing the resistance to fatigue crack propagation (Liu et al., 2008). However, a large number of long needle-like delta phases result in a distinct degradation of the mechanical properties and FCGR (An et al., 2017; Wang et al., 2011). In addition to the δ precipitates, carbides were found to exist, which was confirmed by Energy Dispersive X-Ray Spectroscopy (EDS). The content of the MC carbides in this material was determined to be 2.5 ± 0.5 vol% which is in a good agreement with the value of 1.9 ± 0.5 vol% reported by (Ferreri et al., 2020). γ' and γ'' strengthening phases were not detected due to their nanometre scale sizes. Therefore, further studies in this regard were done using the XRD technique and will be discussed later. In addition, previous research (Ding et al., 2021) showed the presence of the strengthening precipitates in the AM nickel-based alloys after the HT procedures. Using neutron diffraction based procedure, the volume fractions of the γ' and γ'' precipitates of the similar material were determined to be 6.5 ± 1.4 and 8.4 ± 0.3 , respectively (Ferreri et al., 2020).

The SEM micrographs of the HIP+HT IN718 materials, however, captured completely different microstructures, as shown in Fig. 6. The grain elongations in the BD, which were observed in the AP and HT categories, did not exist in the HIP+HT material. Grains were found to be significantly larger, and some twin boundaries were detected. Quantitative details on the grain growth and twin volume fractions will be revealed later in the EBSD part. Comparing the SEM images of the HT

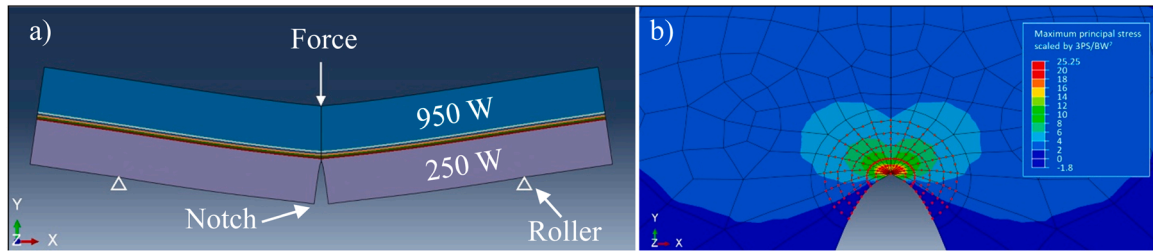


Fig. 2. (a) The FEM model used to calculate the customized K-solutions for the graded materials. (b) The node used to calculate the J integral.

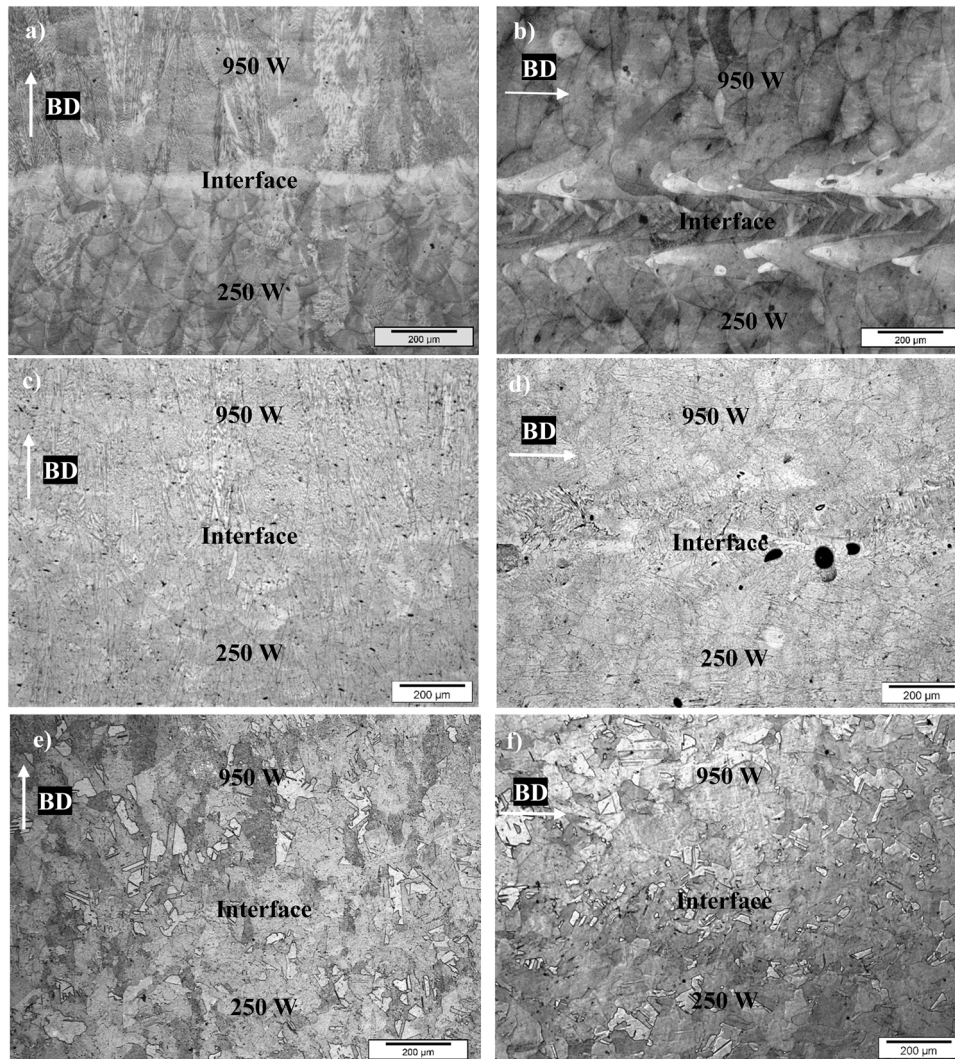


Fig. 3. Optical micrographs of the (a) H-AP, (b) V-AP, (c) H-HT, (d) V-HT, (e) H-HIP+HT, and (f) V-HIP+HT functionally graded samples at the interface area revealing the effect of the various post-processing procedures on the microstructure. The build directions (BD) are indicated in the figures.

and HIP+HT materials, it can be seen that the population of the carbides and δ precipitates is reduced after the HIP+HT procedure. This observation is similar to what was found from the neutron diffraction data on a HIP+HT IN718 superalloy (Ferreri et al., 2020). Similar to the HT category, the existence of the nano-sized γ' and γ'' phases could not be examined using SEM images. Therefore, more analysis using XRD was needed.

The XRD analyses were carried out on the surfaces along the BD to identify the present phases in the AP and post-processed categories. Fig. 7a and b presents the XRD patterns of the 250 W and 950 W-H samples, respectively, in three categories as far as the post treatment

procedure, i.e., AP, HT, HIP+HT. As was expected, the main phase in all categories was the γ phase. In both 250 W and 950 W-H materials, in the AP and HT groups, the relative intensity of the $\gamma(200)$ was higher than the $\gamma(311)$ peak. This can be linked to a preference for growth in $\langle 001 \rangle$ direction and the existence of a strong thermal gradient in the build orientation (Popovich et al., 2017a). In the HIP+HT category, although the intensity of $\gamma(200)$ still remained higher than the $\gamma(311)$ peak, but the preference was not significant. It can be correlated with the grain growth or recrystallization during the HIP procedure (Zhou et al., 2019). The zoomed-in views with identified phases are given in Fig. 7a' and b'. As can be seen, the Laves phase peaks were not detected after the

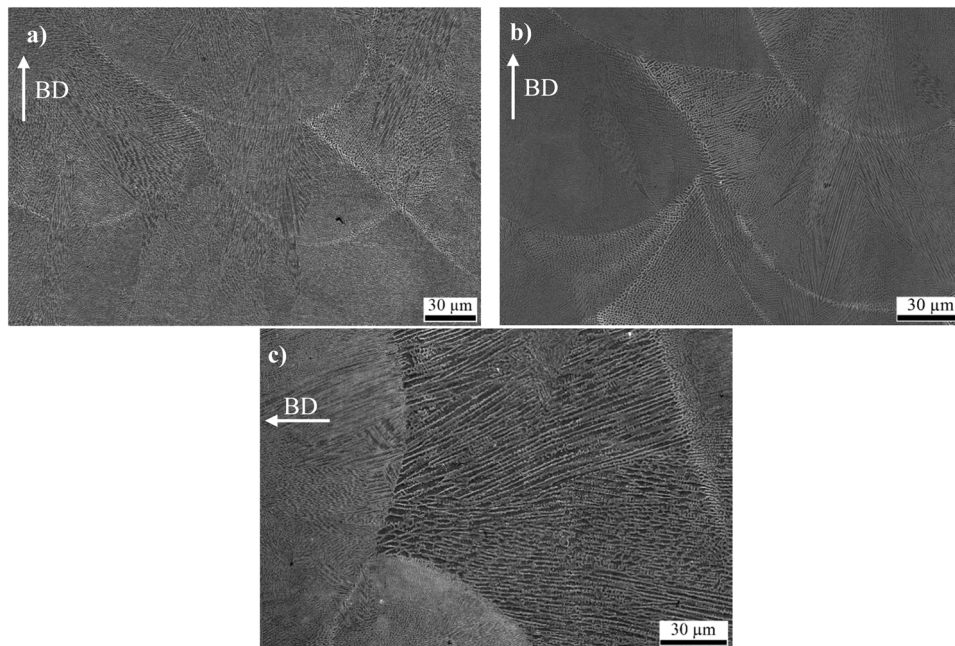


Fig. 4. Microstructure of the AP materials in (a) 250 W, (b) 950 W-H, and (c) 950 W-V conditions captured by SEM technique.

HIP+HT procedure. In addition, the MC carbide peaks, which were present in the HT condition, were reduced in the HIP+HT material. These observations are consistent with what was reported from the neutron diffraction analysis of the L-PBF IN718 after HIP treatment (Ferreri et al., 2020). Moreover, after the heat treatment, δ phase peaks were present in the XRD spectra of 250 W and 950 W-H materials. This is in agreement with the presence of δ precipitates observed in the SEM micrographs given in Fig. 5. The spectra of the HIP+HT samples show a reduction in the precipitates while the carbides are present in the material, as seen in the SEM images in Fig. 6.

To evaluate the effect of the post treatment on the surface hardness of the L-PBF IN718, the Vickers hardness test was performed on the AP, HT, and HIP+HT materials. Fig. 8 shows the average hardness of the NG specimens in different post-processing conditions. It can be seen that the average hardness of all NG categories increased significantly by the HT and HIP+HT procedures, which is attributed to the precipitation of the γ' and γ'' strengthening phases and recrystallization (Komarasamy et al., 2019). Different heat treatment procedures, including solution+aging or homogenization+solution+aging, were reported to increase the hardness of the as processed SLM IN718 by about 30% (Zhang et al., 2015). Similarly, the direct double aging (DA), and solutionizing followed by DA treatments of the laser cladding IN718 coating, were found to increase the hardness significantly due to the precipitation of γ'' and reduction of the Laves phase, respectively (Zhang et al., 2013). The HIP+annealing treatment was found to enhance the Vickers hardness of the SLM IN718 by 46%, while the increase of the hardness by a 4-hour annealing treatment was just below 20% (Amato et al., 2012). It should be noted that the hardness increase by HT was more significant in the 950 W group compared with the 250 W material, where the increase was 51% and 66% for the 950 W-H and 950 W-V, respectively, compared with the 35% rise in the 250 W category. The trend remained the same when the HIP+HT was applied.

Moreover, the Vickers hardness of the FG materials was measured along the height of the samples, including the interface zone. The measurements were done for both vertical and horizontal samples in all studied categories. The hardness profiles of the FG samples measured on the AP, HT, and HIP+HT conditions are provided in Fig. 9. The profiles are averaged over 5 sets of measurements. It can be seen that the hardness values along the samples' height, for H and V orientations, are

close in the HT and HIP+HT categories while are significantly higher than the AP materials. This observation is consistent with the hardness behaviour of the NG materials in different post-processed conditions, given in Fig. 8. In the AP condition, the fit to the hardness profile of the H samples showed a decreasing trend along the height, i.e., parallel to the BD. While in the V samples, the fit along the height, i.e., perpendicular to the BD, remained fairly constant. The average hardness value of the 250 W side of the H sample, which is closer to the build platform (BP), was 361 ± 6 HV, and it was 340 ± 7 HV for the 950 W side, which is the furthest from the BP. This phenomenon is related to the higher number of thermal cycles that the initially deposited layers, which are closer to the BP, i.e., the 950 W side. The repetitive local reheating procedures on the initially deposited layers during the solidification of the latter layers decreases the content of the Laves phase in those layers (Segerstark et al., 2018). Moreover, the reheating cycles can precipitate some content of very small size γ' and γ'' on the initially deposited layers (Tucho et al., 2017). The combination of the mentioned factors resulted in a higher hardness in the 250 W side of the H samples, which was deposited earlier, compared with the other part. On the other hand, the hardness measurements along the height of the V samples were done on the layers which went through the same number of local thermal cycles. As a result, those layers on which the individual sets of hardness measurements were conducted were similar as far as the content of the Laves phase or small strengthening precipitates. Therefore, the hardness value along the height, or the deposition direction, of the V samples remained constant while showed some fluctuations due to the presence of the voids and defects. It should, however, be noted that the hardness values on the AP V samples decreased along the build direction as a consequence of the reduction in the number of the thermal cycles on the previously deposited layers. After post-processing treatments, similar trends were found in the H and V samples, i.e., the hardness of the H samples decreased along the height, and the V samples' hardness was independent of the position along the height. Although, the slope of the hardness decrease in the H samples, lowered which can be related to more homogeneity in the material after post treatment. Another feature which was observed from the hardness profiles of the HIP+HT samples was the reduction in fluctuations compared with the AP and HT samples in both build orientations. This smoothing in the hardness profiles can

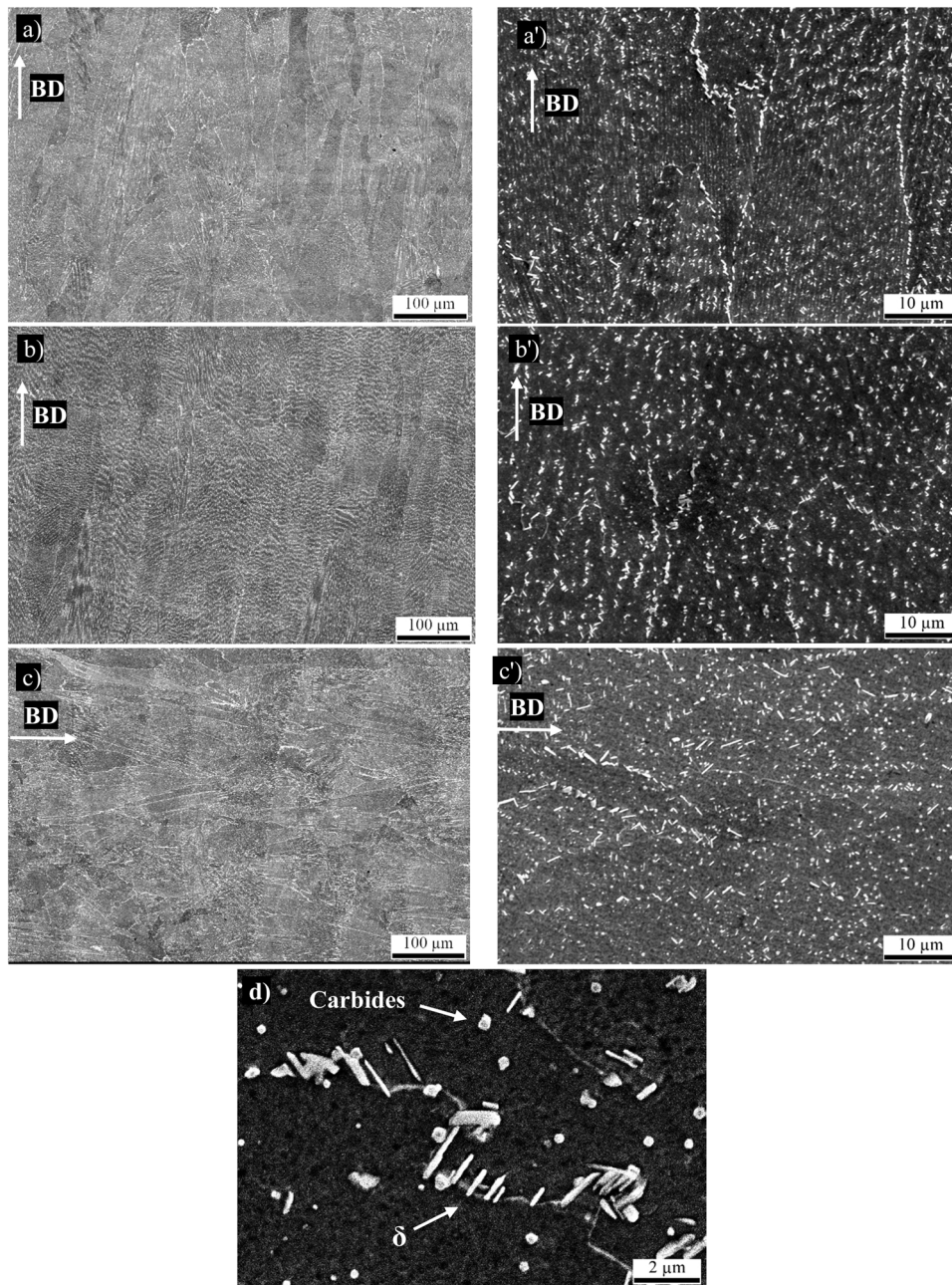


Fig. 5. SEM micrographs of (a) 250 W, (b) 950 W-H, and (c) 950 W-V HT samples. The precipitates are captured in the corresponding higher magnification micrographs provided in sub-figures a'-c', respectively. A higher magnification SEM micrograph of the 950 W-V HT material is provided in (d). The needle shape and globular δ precipitates, and some carbides were located.

be a consequence of fewer defects in the HIP+HT materials.

In addition, the effect of the HT and HIP+HT procedures on the porosity content of the L-PBF IN718 material was measured. Table 5 provides the data regarding the content of the porosity and dimensions of the largest pores found in the AP and post-processed IN718 materials of different manufacturing parameters groups. For a better visualization, the micrographs corresponding to the measurements are given in Fig. 10. As it can be seen, the porosity content of the AP material in 250 W laser power group is lower than the 950 W laser power. Similarly, the average porosity size of the pores was larger in the AP- 950 W material compared with the AP- 250 W material group. These can be related to difference in the combination of heat input and laser scanning speed. In the 250 W materials the heat input and the scanning speed were low which provided sufficient time to complete melting of the

powders. Hence gas entrapment porosity is the major porosity in the 250 W material. Fig. 10 (a) shows the gas entrapment porosity in the 250 W material. In the 950 W category, the heat input was high. Also the scanning speed was correspondingly high. Due to the high scanning speed there was insufficient time for the metal powders to completely melt, which leads to lack of fusion defects as can be seen in Fig. 10 (d).

After HT a slight increase is observed in the porosity content of both laser power categories. This increase could be related to the expansion of the gases entrapped in the gas porosities at high temperatures during the heat treatment. By subjecting the samples to high pressure at high temperature, as done in the HIP treatment, the porosity level is significantly reduced to $0.01\% \pm 0.01$ in 250 W and $0.02\% \pm 0.01$ in the 950 W specimens. Furthermore, the maximum pore size was reduced from $101 \mu\text{m}$ (in AP condition) to $18 \mu\text{m}$ (in HIP condition) for 950 W

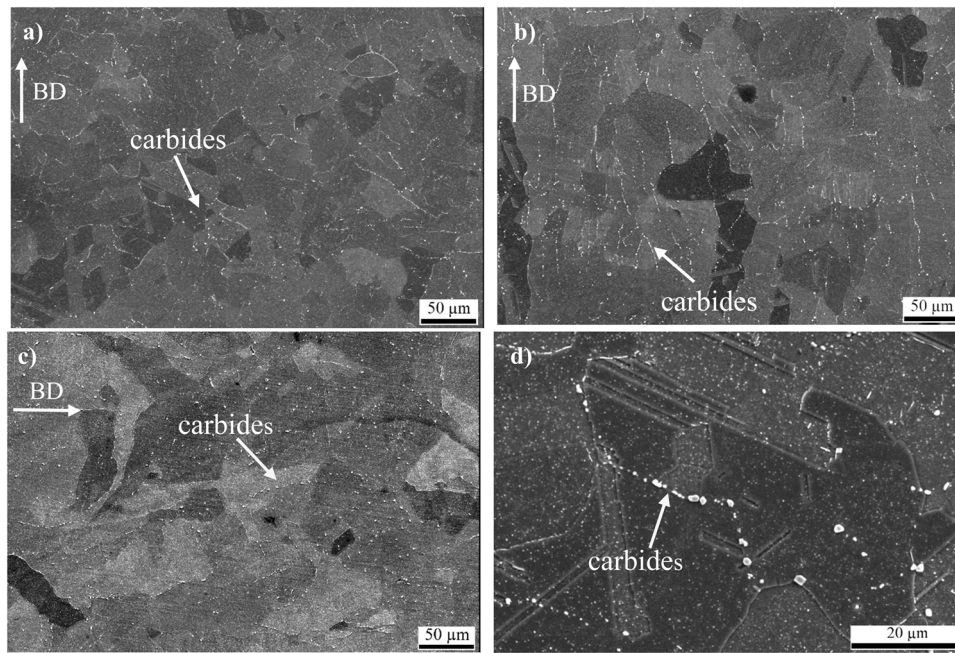


Fig. 6. SEM micrographs on the (a) 250 W, (b) 950 W-H, and (c) 950 W-V samples of the HIP+HT category. The MC carbides were captured in all materials and are more visible in a higher magnification SEM micrograph given in (d), which is taken on the 950 W-H sample.

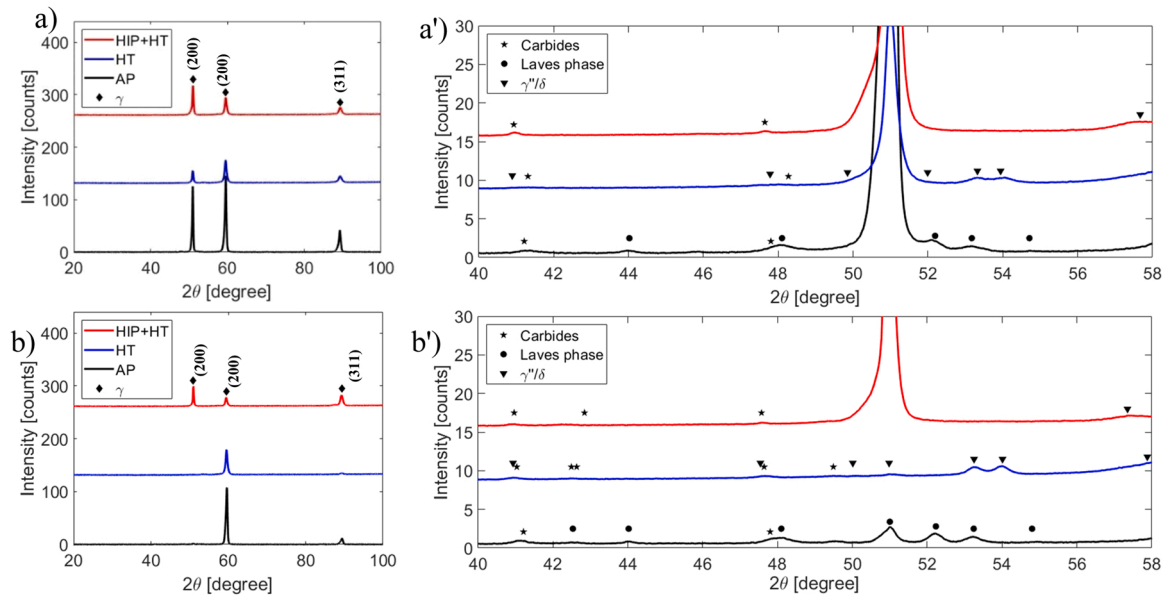


Fig. 7. Phase analyses obtained from XRD on (a) 250 W and (b) 950 W-H categories of AM parts. To better reveal the existing phases, corresponding zoomed-in figures of spectra are provided in (a') and (b') respectively.

samples. The high pressure and temperature thus provide the necessary heat input for the closure of pores. In essence, during HIP the part is subjected to an isostatic pressure on all open surfaces by an inert gas. The high temperature allows the material to flow plastically and close the pores. After enough time the pore surfaces bond together by diffusion and nearly fully close the porosity. However, it is difficult for the entrapped gas to fully escape during the HT process, hence the gas porosities only reduce in size and cannot be completely eliminated. It should be noted that no lack of fusion defect was observed after HIP+HT procedure in neither 250 W nor 950 W materials.

3.2. Evolution of crystallographic texture and grain size

Comprehensive EBSD analyses were conducted on all categories of NG materials to understand the effect of the post-processing treatments on the microstructure and texture of the L-PBF IN718. Figs. 11 and 12 present the inverse pole figure (IPF) maps, pole figures, and the misorientation angle plots for the AP, HT, and HIP+HT materials. From the IPF maps it can be seen that the AP and HT materials have columnar grains extended along the build directions, while the grains of the HIP+HT do not show any preferential orientation. The elongation of the columnar grains of the AP and HT samples was dependent on the laser parameters and build orientations. For easier comparison, the data describing the shapes of the grains are summarized in Table 6. It should

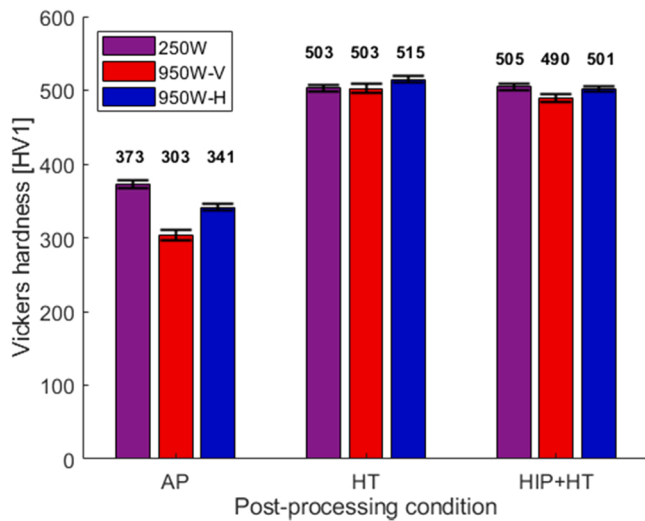


Fig. 8. Bar graphs showing the average Vickers hardness values of the non-graded L-PBF materials manufactured using different parameters. The graphs are plotted for as-processed (AP), heat treated (HT), and hot isostatic pressed and heat treated conditions (HIP+HT).

be mentioned that the pole figures and the grain shape statistics are calculated from multiple EBSD imaging on the same sample to have a sufficient number of grains representing the material structure. In the AP group, the grain size and elongation of the 250 W and 950 W-V materials were close with aspect ratios of 0.27 and 0.25 and the major axis of 135.6 μm and 147.7 μm , respectively. Although their grains were columnar, the elongation was less compared with the 950 W-H sample with an aspect ratio of 0.18 and a major axis of 518.4 μm . These differences can be generated by the heat flow, which is parallel to the build direction and introduces the preferred grain orientation (Kreitzberg et al., 2017). Observing the IPFs of the HT materials, it is evident that the 250 W and 950 W-V materials experienced grain growth and became even more elongated, i.e., a reduction in the aspect ratios. The grain growth caused by HT can be linked to the grain boundary migration caused by atoms diffusion (Holland et al., 2018). The 950 W-H material, which had the largest and most elongated grains in the AP condition, however, showed a reduction in the grain size and a tendency to become more equiaxed, where the aspect ratio increased from 0.18 to 0.2. Similar behaviour of the reduction in grain size after stress relief annealing treatment of an L-PBF IN625 (Kreitzberg et al., 2017) and 2-h and 6-h heat treatment of L-PBF MAR-M-509 (Ferreri et al., 2019) were reported. Moreover, as it will be discussed in the following parts, the

residual stress of the 950 W-H samples was found to be higher than the 950 W-V specimens. The residual stresses caused by the thermal cycles are considered as the driving forces of recrystallization in IN718 (Liu et al., 2011). This can influence the grain size evolution after the HT process.

Grains had a totally different microstructure after the HIP+HT procedure. As the IPFs in Fig. 11 g-i demonstrate, the grains were not as extended along the BD as the AP and HT categories and were oriented randomly. The IPFs and grains' statistics listed in Table 6 show that all categories had grain growth and recrystallization after HIP+HT. The 250 W and the 950 W-H microstructures show more equiaxed grains while still, some extent of elongation is present in the 950 W-V sample. Another feature of the IPFs is the presence of the annealing twin boundaries in the HIP+HT materials. The $\Sigma 3$ twins are defined as boundaries with 60° misorientations along the $\langle 111 \rangle$ orientation (Blochwitz and Tirschler, 2005). Equiaxed grains with annealing twin boundaries define a low stacking fault energy matrix. Blank IPFs highlighting the grain boundaries and $\Sigma 3$ twin boundaries are provided in Fig. 13. While the HIP+HT samples, especially the 250 W and 950 W-H groups, contained significant amounts of twin boundaries, considerable annealing twin boundaries were not found in the AP and HT samples. This is in agreement with the misorientation angle plots given in 12, where the annealing twins have the 60° misorientation angle. The formation of incoherent annealing twins after HIP treatment on the L-PBF nickel-based superalloys was reported in other research (Kreitzberg et al., 2017). The low angle grain boundaries (angles $<15^\circ$ (Tochigi et al., 2018)) were present in the AP material. They are formed by arrays of dislocations as consequences of rapid solidification and the fact that during solidification, sub-grains grow along the proffered crystallographic direction, i.e., $\langle 100 \rangle$ for the FCC materials (Marchese et al., 2020). The presence of LAGB, which can be an indication of the extent of local deformation or residual stresses, was reported in the L-PBF

Table 5

A summary of the porosity content and the largest pore size measured on AP and treated IN718 materials produced using 250 W and 950 W laser powers.

| Material category | Porosity content [%] | Largest porosity diameter [μm] | Average porosity diameter [μm] |
|-------------------|----------------------|---|---|
| 250 W- AP | 0.13 ± 0.04 | 74 | 14.5 ± 7.8 |
| 250 W- HT | 0.18 ± 0.03 | 77 | 15.2 ± 10.3 |
| 250 W- HIP+HT | 0.01 ± 0.01 | 13 | 9.1 ± 1.7 |
| 950 W- AP | 0.21 ± 0.07 | 101 | 18.7 ± 11.3 |
| 950 W- HT | 0.26 ± 0.1 | 104 | 19.5 ± 10.4 |
| 950 W- HIP+HT | 0.02 ± 0.01 | 18 | 10.4 ± 3.2 |

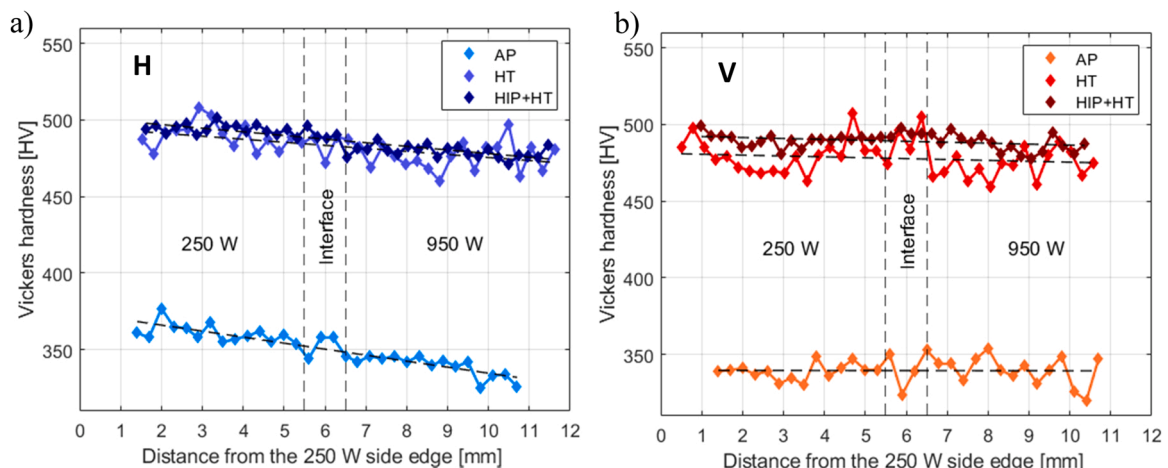


Fig. 9. Hardness profiles of (a) horizontal and (b) vertical functionally graded samples in different post-processing conditions.

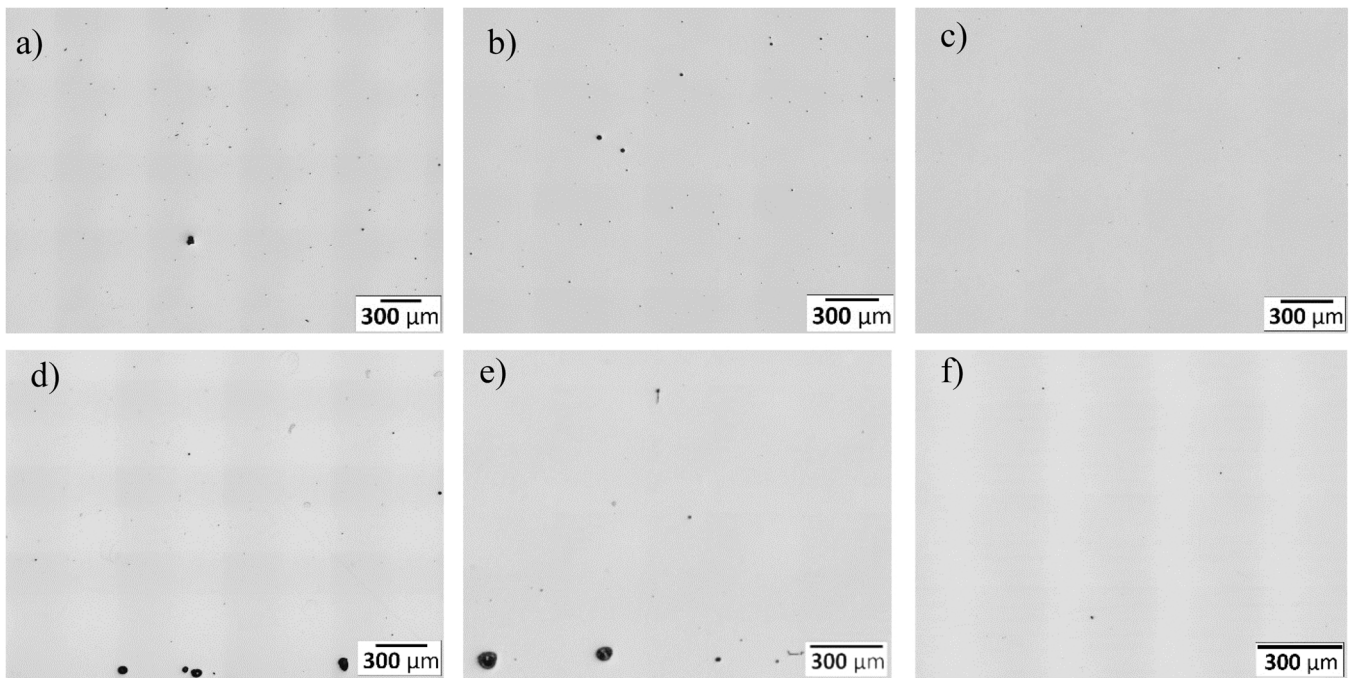


Fig. 10. micrographs showing porosity analysis on (a) 250 W- AP, (b) 250 W- HT, (c) 250 W- HIP+HT, (d) 950 W- H- AP, (e) 950 W- H- HT, and (f) 950 W- H- HIP+HT materials. It can be seen that the HIP+HT materials in both laser powers show the least amount of porosity with no lack of fusion defects.

nickel-based superalloys such as Inconel 718, Inconel 939 (Kanagarajah et al., 2013), and Inconel 625 (Kreitzberg et al., 2017). Their fractions after HIP+HT were found to be less than those in the AP condition. The reduction in LAGB content was more pronounced for the 250 W and 950 W-H, which had more annealing twins after the HIP+HT process (see Fig. 13 g-i). It is related to the recrystallization and formation of the $\Sigma 3$ twin boundaries and high angle grain boundaries. Similar behaviour was reported after post-processing of the AM nickel-based superalloys in previous research on Inconel 625 (Marchese et al., 2020) and Inconel 718 (Smith et al., 2016).

The stereographic pole figures with triclinic symmetry of NG materials in AP, HT, and HIP+HT conditions are plotted in 12. Pole figures were constructed employing an orientation distribution function. Additively manufactured nickel-based superalloys are expected to possess either a Goss texture component ($\{110\}\langle 100\rangle$) or a cubic texture component $\{001\}\langle 100\rangle$ which originate from the solidification of $\langle 100\rangle$ -oriented grains or dendrites and is affected by the processing parameters (Ma et al., 2017). Fig. 12 a-c provides the crystallographic textures of the AP materials. The 250 W IN718 showed a weak Goss texture with a maximum multiples of random distribution (m.r.d.) of 3.4. The texture derived for the 950 W- H sample, however, was a strong cubic texture with a maximum m.r.d. intensity of 17.2. The 950 W- V material had a moderate texture. Strong $\langle 001\rangle$ fibre textures in the AM IN718 built with the higher laser power of 950 W, compared with a near random texture in the lower laser power builds, i.e., 250 W, was observed. Applying the heat treatment, the 250 W material's texture evolved to $\langle 001\rangle$ fibre, and the intensity showed a slight increase but remained moderate. Similarly, the 950 W- V material had a fibre texture after HT, but the increase in the intensity was significant, and the maximum value of m.r.d. was about 27, which was the strongest in all HT parts. The formation of $\langle 001\rangle$ fibre texture after HT was observed in other research (Kreitzberg et al., 2017). The crystallographic texture of the 950 W- H material remained similar to the AP condition with slight spreads. The intensity showed a modest decrease but remained strong with a value just below 16. In the HT materials, the intensity of the $\langle 001\rangle$ was found to be high, especially for 950 W materials compared with the 250 W. This behaviour is in line with what was detected by XRD, where

the intensity of $\gamma(200)$ remained higher than $\gamma(311)$. The HIP+HT procedure changed the microstructure of the horizontal samples significantly. Both 250 W and 950 W-H materials exhibited random textures with weak intensities. The decrease in the maximum intensity of the H samples is consistent with the less difference in the $\gamma(311)$ and $\gamma(311)$ peaks of the XRD spectra. The 950 W- V sample, however, behaved differently after the HIP+HT. The texture was cubic-like, and the maximum intensity increased to about 13.

Lastly, using the measured EBSD data, the grain orientation spread (GOS) maps were plotted for all categories of materials. Fig. 14 shows the GOS maps of the 250 W, 290 W- H, and 290 W-V materials in AP, HT, and HIP+HT conditions. The average GOS and the maximum GOS values of each plot are also provided. The GOS plots give an indication of intragranular distortions and also of the residual stress in the material where higher GOS values imply higher misorientations and residual stress (Zhao et al., 2020). Comparing the GOS plots of the 250 W materials, the average values reduced after both HT and HIP+HT, which means the residual stresses decreased after post-processing. The trends were different for the higher laser power samples. It should be noted that the residual stress of the 950 W samples varied depending on the build orientation. It can be a consequence of more free surfaces or free edges of the vertical compared with the horizontal specimens. In addition, the distance from the build platform on the V and H samples were different. These factors can end up in different thermal profiles in different build directions, which influences the residual stress values. While the average GOS of the 950 W- H material remained almost the same after post-processing treatments, the maximum GOS increased after HT and decreased significantly from 27.13° in AP to 4.83° in the HIP+HT condition. The average GOS of the 950 W- V samples was measured to be 0.88° in the AP condition, and it decreased to 0.58° after the HT procedure. While the maximum GOS of the HIP+HT material decreased to 10.26° , compared with the 50.73° in the AP condition, its average GOS increased to 1.14° , which shows a higher residual stress value.

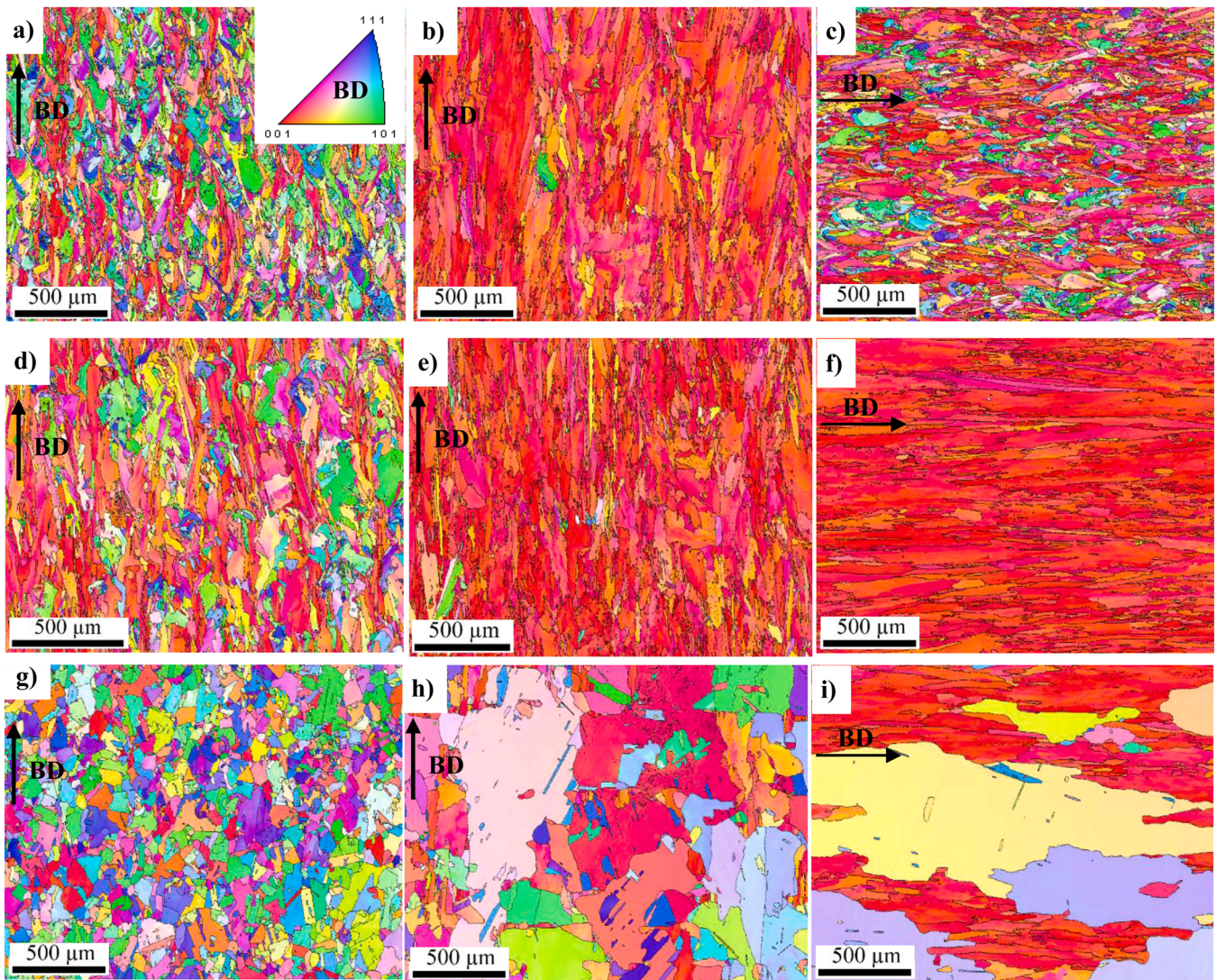


Fig. 11. Inverse pole figure maps of different categories of materials explored in this study prior to the fatigue testing. The EBSD imaging was done on large areas of (a) 250 W- AP, (b) 950 W- H- AP, (c) 950 W- V- AP, reproduced from (Ghorbanpour et al., 2021), (d) 250 W- HT, (e) 950 W- H- HT, (f) 950 W- V- HT, (g) 250 W- HIP+HT, (h) 950 W- H- HIP+HT, and (i) 950 W- V- HIP+HT materials. (c) Reproduced from (Ghorbanpour et al., 2021).

3.3. Mechanical properties

3.3.1. Fatigue behaviour of non-graded (NG) material

The effects of the different post processing procedures on the microstructure were explored in the previous section. The results of two types of fatigue crack growth parameters, namely the stress intensity range threshold (ΔK_{th}) and the Paris law crack growth, are discussed in this part.

Stress ratio, $R=0.7$.

To find out the influence of the microstructure on the crack propagation behaviour, constant K_{max} experiments were conducted on the NG and wrought-HT parts. The starting stress ratios were set to 0.1, and the final stress ratios were about 0.6–0.7. ΔK_{th} values obtained for different categories of tested materials are listed in Table 7. It should be noted that the K_{max} value for all tests was $25 \text{ MPa}\sqrt{m}$. In the AP category, the ΔK_{th} values were close, while the 250 W material had the highest threshold stress intensity factor (SIF) range followed closely by the 950 W- V samples. This behaviour can be a consequence of the different grain sizes in the tested materials. It is known that more grain boundaries or finer grains hinder crack growth (Hornbogen and Gahr, 1976). On the other hand, large grains are capable of accommodating more slip

damage due to their fewer constraint to slip compared with the small grains, which can result in a higher ΔK_{th} value (Toh and Rainforth, 1996). So, as suggested in the literature, the relationship between the grain size and the threshold SIF range is influenced by different competing parameters (King, 1982). In addition, at low stress ratios, roughness-induced crack closure in the coarse grains can induce an overall better near threshold crack growth behaviour (Yamada and Newman, 2009). Finer-grained microstructure on the other hand can lead to a straighter crack with lower surface roughness, which reduces the effects of crack tortuosity and roughness-induced crack closure and hence lessens the fatigue overload retardation effects. From the microstructural analysis, AP-250 W material had the finest grains, followed by the 950 W- V category. Moreover, the orientations of the grains in the 950 W- V parts created more grain boundaries in front of the crack path.

For the HT materials category, the ΔK_{th} values increased compared with the AP materials. This improvement in the threshold SIF range is associated with the presence of the strengthening phases, which precipitated after the HT process. Similar to the AP category, the 250 W samples showed the highest ΔK_{th} due to possessing the finest grains in their microstructure, which adds up the grain boundaries in front of the crack path. The ΔK_{th} of a laser directed energy deposited (LDED) IN718

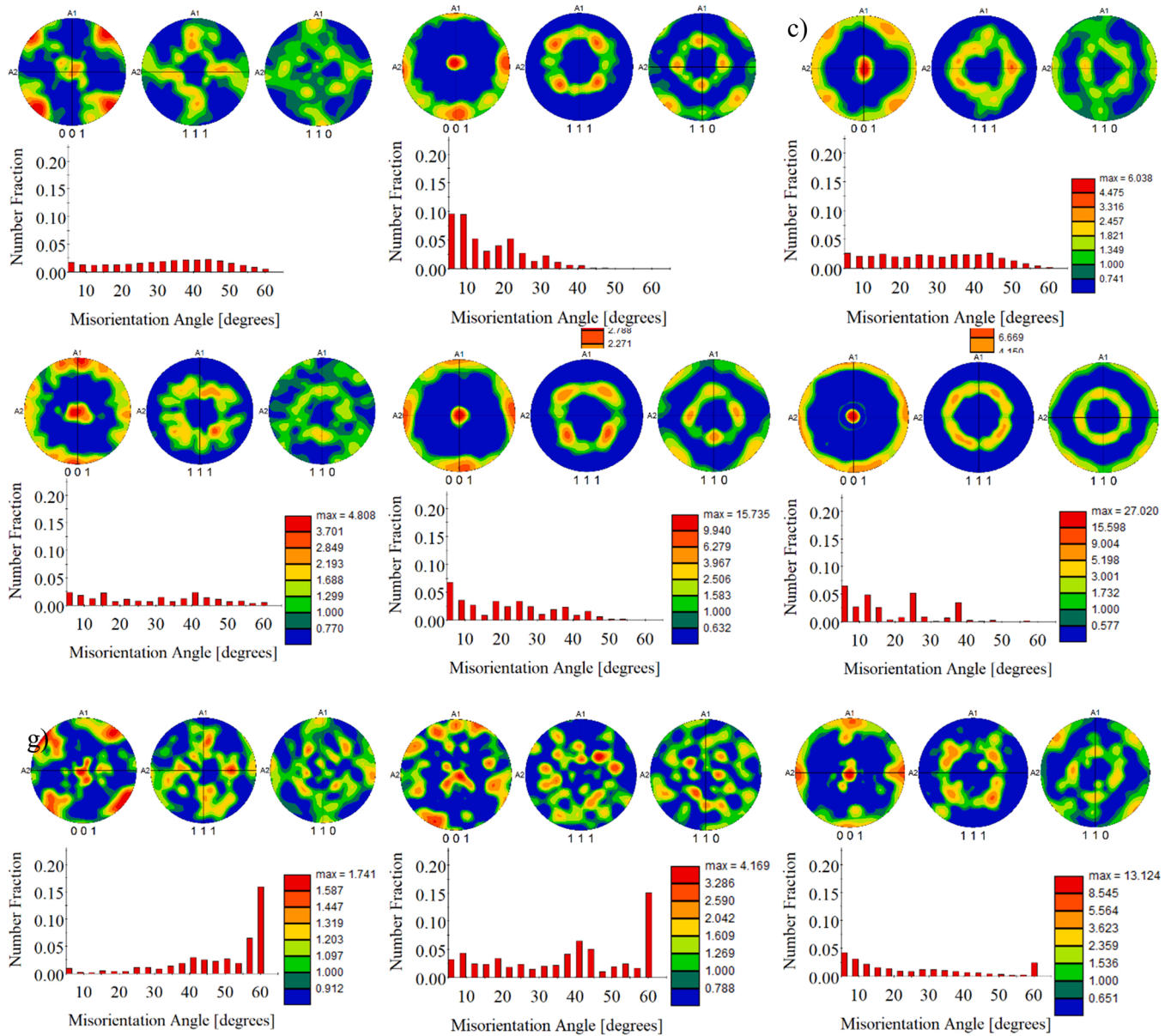


Fig. 12. Pole figures and misorientation angles corresponding to the IPFs provided in Fig. 10 as (a) 250 W- AP, (b) 950 W- H- AP, (c) 950 W- V- AP (d) 250 W- HT, (e) 950 W- H- HT, (f) 950 W- V- HT, (g) 250 W- HIP+HT, (h) 950 W- H- HIP+HT, and (i) 950 W- V- HIP+HT materials. In all pole figures the build direction is parallel to the A3 (the out of the plane direction). Note that the misorientation angles lower than 5° are not included in the misorientation plots.

Reproduced from Ghorbanpour et al., 2021

Table 6

Grain shape statistics of different NG materials obtained from multiple EBSD imaging.

| Material category | 250 W | | | 950 W- H | | | 950 W- V | | |
|-------------------|-------|-------|--------|----------|-------|--------|----------|-------|--------|
| | AP | HT | HIP+HT | AP | HT | HIP+HT | AP | HT | HIP+HT |
| Minor axis [μm] | 28.9 | 35.9 | 55.1 | 79.9 | 58 | 181.3 | 27.3 | 103 | 113.5 |
| Major axis [μm] | 135.6 | 203.9 | 141.7 | 518.4 | 335.5 | 582.3 | 147.7 | 938.9 | 719.2 |
| Aspect ratio | 0.27 | 0.24 | 0.41 | 0.18 | 0.2 | 0.36 | 0.25 | 0.12 | 0.18 |

after a similar HT to this study was reported to be $10.8 \pm 0.1 \text{ MPa}\sqrt{m}$ (Yu et al., 2021). Comparing the wrought-HT and L-PBF- HT materials, it turned out that the ΔK_{th} of the wrought samples were higher, which can be associated with their equiaxed fine grains with major axes of less than 20 μm. The threshold SIF range of a solutionized and double-aged extruded Inconel 706, at R= 0.8, was reported to be in the range of 5.7–13.9 $\text{MPa}\sqrt{m}$ in different directions (Liaw and Logsdon, 1988). In

the HIP+HT category, the grain size increased, which could affect the ΔK_{th} . Also, the strengthening precipitates were present in the materials compared with the AP condition. Additionally, the content of the porosity in the HIP+HT material was found to be less than the AP and HT samples (Popovich et al., 2017b), which can increase the ΔK_{th} value. As a result, after HIP+HT, all materials showed an increase in the threshold SIF range, with the 950 W- H samples having the highest ΔK_{th}

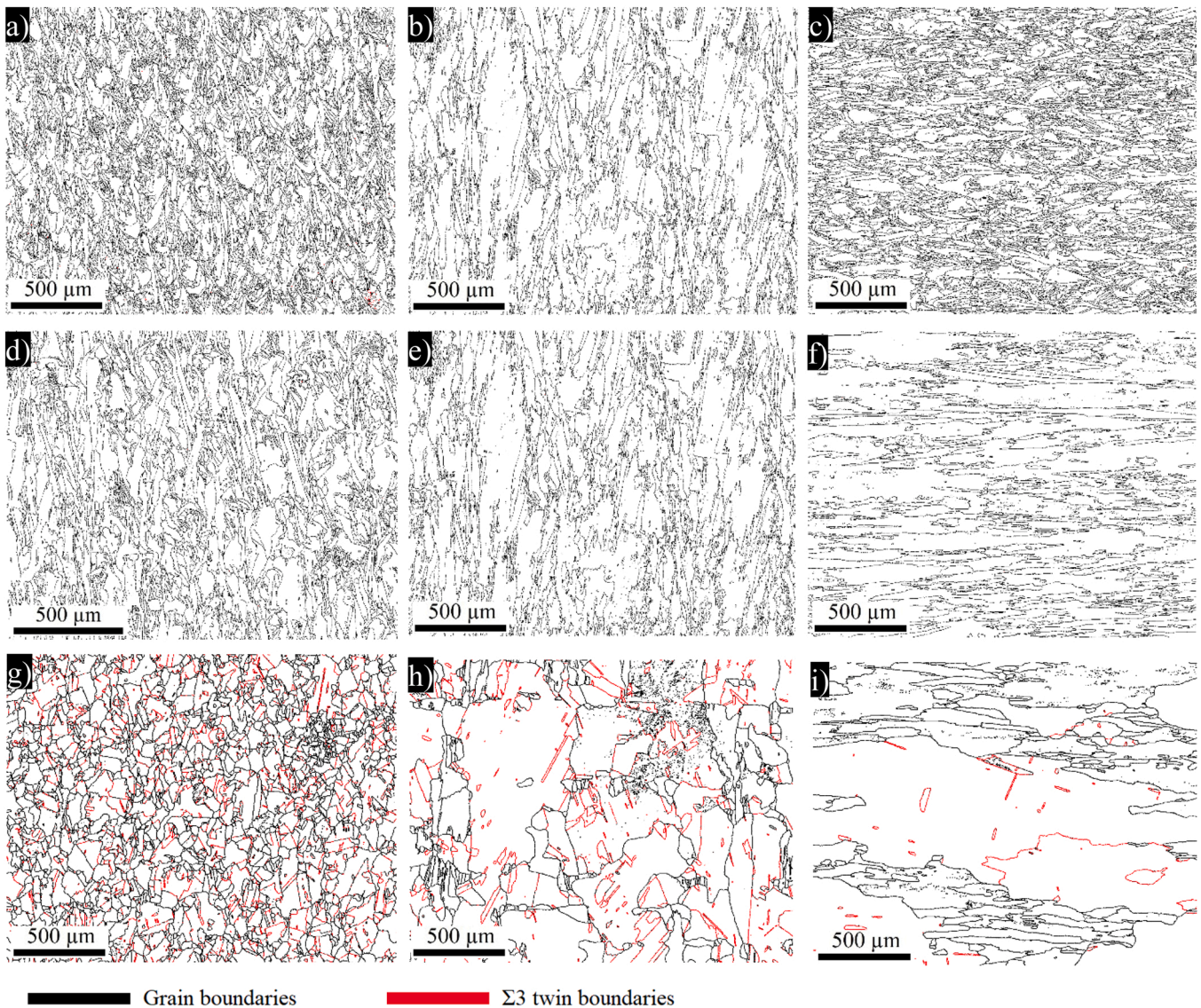


Fig. 13. Blank maps identifying the grain boundaries in black, and annealing twin boundaries, in red. The blank maps a-i correspond to the IPFs provided in Fig. 11. (For interpretation of the references to colour in this figure legend, the reader is referred to the web version of this article.)

values. The high threshold SIF range value of these categories can be a consequence of the formation of annealing twins as the annealing twin boundaries can act as dislocation barriers in the early stages of the crack growth (Toh and Rainforth, 1996).

Stress ratio, $R=0.1$.

Furthermore, the K_{max} constant tests of the NG and wrought-HT materials were conducted at a constant stress ratio of $R=0.1$, i.e., compared with the increasing R ratio in the previous section. Fig. 15 gives the fatigue crack growth rate, da/dN , versus SIF range, ΔK , curves plotted for AP, HT, and HIP+HT samples. In addition to the curves based on the collected data points, the fits to the measured curves are provided. Eq. 5 (Paris and Erdogan, 1963), which has two empirical constants, namely Paris exponent, m , and Paris constant, C , was used for fitting purposes.

$$\frac{da}{dN} = C(\Delta K)^m \quad (5)$$

Table 8 lists the empirical constants of the Paris curves and the threshold SIF range values of all curves, plotted in Fig. 15. It should be mentioned that the ΔK_{th} values from the Paris curves are slightly different from those which are provided in Table 8. The differences are

related to the different stress ratios (R) in the tests, which alter the crack closure phenomenon. In the coarse grains, the roughness induced crack closure is supposed to improve the fatigue crack growth behaviour. However, in the HT materials, which still remained directional, the orientations of the grains and their elongation direction with respect to the crack direction played an important role. For instance, in the 950 W-H samples, the large axes of the grains, i.e., $336 \mu\text{m}$, faced the crack path while it was the short axes, i.e., $103 \mu\text{m}$, in the 950 W-V samples. Even in the lower laser power samples, the axes of the grains facing the crack were about two times the 950 W-V specimens. Therefore, a higher roughness induced crack closure effect in the H samples was expected. Changes in the threshold SIF range values depending on the stress ratios were observed in Inconel 625 (Hu et al., 2020b) and Inconel 718 (Newman and Yamada, 2010). Increasing the stress ratio from 0.1 to 0.7 in a wrought IN718, which was solutionized at $1050 \text{ }^\circ\text{C}$ for 1 h and double aged analogous to the double-aging procedure of the wrought material in this study, decreased the ΔK_{th} from 10.2 to $5.8 \text{ MPa}\sqrt{\text{m}}$ (Li et al., 2018).

Based on the previous research, the fatigue crack growth resistance of the AM IN718 is remarkably lower than the conventional materials, which can be caused by the higher residual stress and the microstruc-

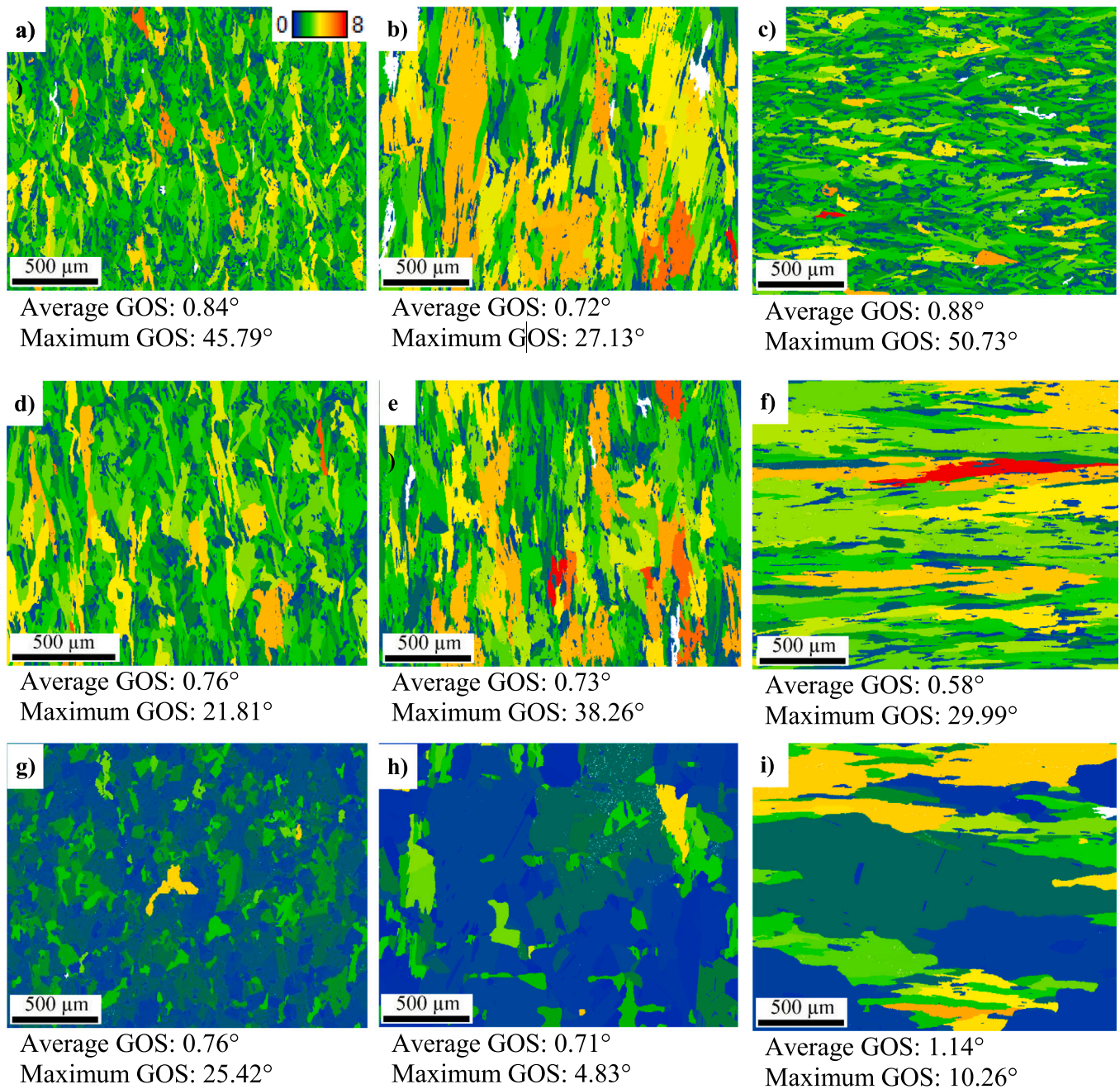


Fig. 14. Grain orientation spread (GOS) of (a) 250 W- AP, (b) 950 W- H- AP, (c) 950 W- V- AP, (d) 250 W- HT, (e) 950 W- H- HT, (f) 950 W- V- HT, (g) 250 W- HIP+H, (h) 950 W- H- HIP+H, and (i) 950 W- V- HIP+H samples. The values of average GOS and maximum GOS of each plot are provided. The colour-bar provided in (a) applies to all plots.

Table 7

A summary of constant K_{\max} tests performed on the NG-HT, NG-HIP+HT, and wrought-HT samples to obtain the ΔK_{th} values.

| Processing condition | Sample category | Final stress ratio | ΔK_{th} [MPa \sqrt{m}] |
|----------------------|-----------------|--------------------|-----------------------------------|
| L-PBF- AP | 250 W | 0.7 | 7.2 ± 0.3 |
| | 950 W- H | 0.7 | 6.0 ± 0.2 |
| | 950 W- V | 0.7 | 7.0 ± 0.3 |
| L-PBF- HT | 250 W | 0.7 | 9.5 ± 0.2 |
| | 950 W- H | 0.7 | 7.9 ± 0.2 |
| | 950 W- V | 0.7 | 7.5 ± 0.3 |
| L-PBF- HIP+HT | 250 W | 0.7 | 7.7 ± 0.3 |
| | 950 W- H | 0.6 | 10.2 ± 0.2 |
| | 950 W- V | 0.7 | 8.8 ± 0.2 |
| Wrought-HT | – | 0.6 | 13.1 ± 0.9 |

tural specifications of the AM parts (Konečná et al., 2016). However, proper post-processing treatments can improve the FCG behaviour of the AM parts and make it comparable with the wrought material. Comparing the HT curves, it can be seen that the fatigue crack growth rate (FCGR) of the HT L-PBF parts is still higher than the wrought material. Moreover, the ΔK_{th} of the wrought samples, 15.1 ± 2.4 MPa \sqrt{m} , are significantly higher than the L-PBF specimens ranging around 7–11 MPa \sqrt{m} . The ΔK_{th} of a laser directed energy deposited (LDED) IN718 with similar HT as the current study, found to be 10.8

± 0.1 MPa \sqrt{m} (Yu et al., 2021), which is in good agreement with the findings of this study. However, in the mentioned study (Yu et al., 2021), the FCGR of the HT LDED material was found to be consistent with the wrought ones, which was relatively weaker compared with the wrought

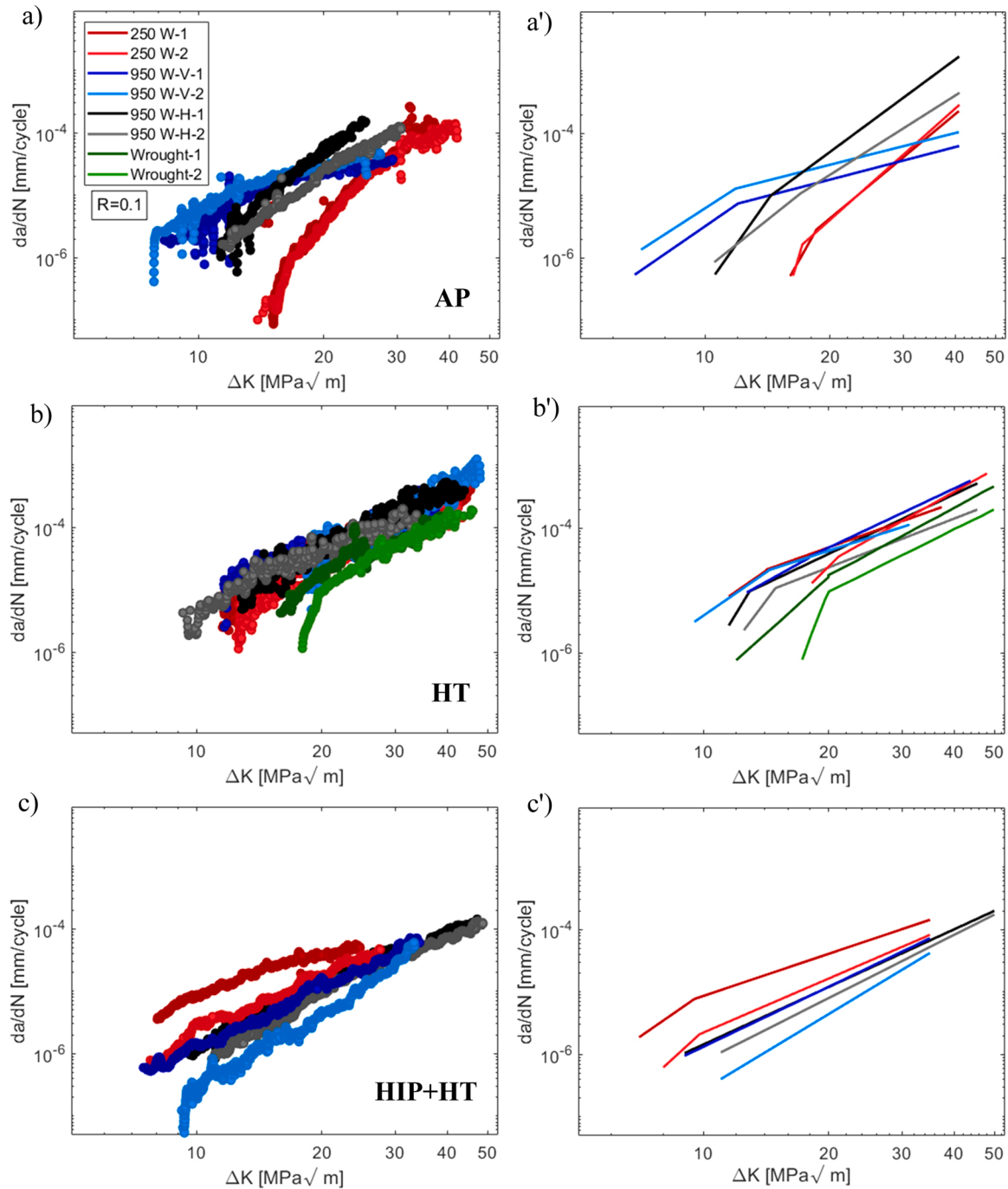


Fig. 15. Fatigue crack growth curves of non-graded samples measured in (a) AP (b) HT and (c) HIP+HT conditions at a stress ratio of $R=0.1$. The corresponding Paris law fits are provided in (a'), (b'), and (c'), respectively. The legend given in (a) applies to all plots.

(a) Reproduced from (Ghorbanpour et al., 2021).

samples in the current research. Fig. 15 b and b' give the HIP+HT samples' curves. Putting them up against their HT counterparts, it is evident that the FCGR decreased significantly, resulting in a better performance than the wrought-HT samples. The improvement in the fatigue behaviour can be related to the crack tip blunting caused by the carbides present at the grain boundary, shown in Fig. 6, similar to what was reported in HT Inconel 690 (Park et al., 1996). The ΔK_{th} of both 950 W categories increased after HIP+HT compared with the AP materials. However, they still did not reach the ΔK_{th} of the wrought-HT samples explored in our research. The increase in the threshold SIF range values after HIP+HT can be related to the decrease in the residual stress and defects such as porosities which were induced during the

manufacturing process. Furthermore, after the HIP+HT procedure, the texture in all categories became more isotropic, and grain growth was observed, which is known to hinder fatigue crack propagation (Hu et al., 2021). It should also be noted that ΔK_{th} of the HIP+HT samples was not affected by the crack-closure. In Fig. 15, it can be seen that the FCGR decreased after post processing and it was more pronounced in the HIP+HT category. The 0.2% yield strength of the 250 W and 950 W laser power categories were measured to be 668 ± 16 and 531 ± 9 MPa, respectively (Popovich et al., 2017b). The values increased to 1145 ± 16 and 1065 ± 20 MPa after HIP+HT (Popovich et al., 2017b). The lower FCGR in the parts with higher yield strength after heat treatment procedures is consistent with an earlier report (Yu et al., 2020).

Table 8

A summary of Paris law constants for L-PBF non-graded AP, HT, HIP+HT, and wrought-HT samples tested at $R=0.1$. The ΔK_{th} values are calculated at FCGR of 10–6 mm/cycles. The AP and wrought-HT fatigue data are taken from our previous work (Ghorbanpour et al., 2021) for comparative study.

| Processing condition | | ΔK_{th} [MPa \sqrt{m}] | Paris exponent (m_1) | Paris exponent (m_2) | Paris constant (C_1) | Paris constant (C_2) |
|----------------------|----------|-----------------------------------|--------------------------|--------------------------|--------------------------|--------------------------|
| AP | 250 W | 16.5 ± 0.1 | 5.7 ± 0.1 | – | (1.6 ± 0.5) E-13 | – |
| | 950 W- H | 9.2 ± 0.2 | 4.6 ± 0.8 | – | (1.2 ± 1.1) E-10 | – |
| | 950 W- V | 6.0 ± 0.5 | 3.0 ± 0.1 | 1.1 ± 0.2 | (6.0 ± 2.3) E-9 | (9.4 ± 4.3) E-7 |
| HT | 250 W | 10.9 ± 0.5 | 9.9 ± 1.0 | 2.9 ± 0.3 | (2.0 ± 1.95) E-16 | (6.5 ± 3.5) E-9 |
| | 950 W- H | 7.2 ± 0.2 | 4.2 ± 0.4 | 2.6 ± 0.5 | (4.2 ± 3.2) E-10 | (7.4 ± 0.4) E-8 |
| | 950 W- V | 9.9 ± 2.5 | 5.6 ± 1.0 | 3.1 ± 0.7 | (5.0 ± 4.9) E-11 | (2.0 ± 1.9) E-8 |
| HIP+HT | 250 W | 9.8 ± 0.9 | 3.2 ± 0.2 | – | (8.0 ± 4.6) E-10 | – |
| | 950 W- H | 11.5 ± 2.3 | 3.6 ± 0.4 | – | (4.4 ± 4.2) E-10 | – |
| | 950 W- V | 7.4 ± 1.3 | 5.4 ± 0.7 | 2.6 ± 0.3 | (1.2 ± 1.1) E-10 | (2.7 ± 2.4) E-8 |
| Wrought- HT | | 15.1 ± 2.4 | 11.3 ± 5.7 | 6.1 ± 0.1 | (4.5 ± 4.5) E-13 | (3.5 ± 1.1) E-10 |

3.3.2. Fatigue behaviour of functionally graded (FG) materials

One of the main purposes of the current study was to explore the fatigue behaviour of the FG materials which was possible by conducting the ΔK -constant tests. Prior to performing the ΔK -constant tests on the FG parts, customized K solutions were obtained using an FEM model. The K values were calculated for different crack lengths between 1.5 mm and 7.5 mm, along the width of the samples. The calculations were done with crack length interval of 0.5 mm when the potential crack was far enough from the interface and 0.2 mm in zones closer to the interface. Fig. 16-a shows the calculated SIF values for AP and post-processed FG materials, along with the K values calculated according to ISO 12135 (ISO, 2016) for the NG materials. To make an easier comparison, the values of the SIF of the FGMs are normalized by the K values calculated based on the standard. The normalized plots are provided in Fig. 16-b. From the plots, it can be seen that due to the presence of the interface zone, the K values of the graded parts are higher than that of the non-graded materials. The largest difference in the K values of the FG parts and the NG material calculated from the standard was observed in the AP group, while the HIP+HT category showed the least deviation. When the crack tip was about to reach the interface, all FG curves showed the most noticeable variance from the standard curve calculated for the NG material. After crack enters the interface, the effect of the interface on K starts to reduce in all samples. Quickly after the crack passes to the other region, the K values of the FG and NG parts converge.

Having the customized K solutions calculated, ΔK -constant tests were carried out on the FG materials. Fig. 17 provides the FCGR, da/dN , against the crack length, a , for different sample orientations in HT and HIP+HT conditions. Also, the dashed lines represent the fits to the AP curves, which are discussed in more details in our previous research

(Ghorbanpour et al., 2021). It should be noted that all samples were tested at $\Delta K=22.5$ MPa \sqrt{m} .

The FCGR of HT and HIP+HT samples in both directions found to be approximately constant along the width of the samples as the crack propagated. The FCGR fluctuated between 2E-5 and 5.5E-5 mm/cycle in the HT and 2.3E-5–6.9E-5 mm/cycle in the HIP+HT conditions, which are considered as close ranges. This observation in the FCGR of the FG samples after HT and HIP+HT is similar to their hardness behaviour. The horizontal direction samples exhibited a slightly lower da/dN , which could be related to their relatively moderate texture. The AP- H samples showed a different fatigue behaviour, with FCGR starting from 4E-6 mm/cycle, which was lower than the other samples and gradually increasing to about 7.2E-5 mm/cycle. This gradual increase in the FCGR arises from the different number of thermal cycles and consequently various fractions of the Laves phases and possible strengthening precipitates in the deposited layers closer to the build platform, i.e., the 250 W side, and those layers which are further from the build platform, i.e., the 950 W side. This behaviour is consistent with the hardness of the graded H samples. After post processing, the microstructure becomes more uniform with a more homogenous distribution of the precipitates so the gradual change in FCGR was not observed. The minimum FCGR of the AP- H material, 4E-6 mm/cycle, was lower than the post processed samples. This can be related to differences in compressive RS as they are known to act as extrinsic crack closure factors (Li et al., 2018). The average GOS of the 250 W samples found to be lower after HT and HIP+HT compared with the AP materials (see Fig. 14). This is an indication of the reduction in the RS values after post-processing treatments. To confirm this quantitatively, the residual stress measurements using the XRD technique were done on the 250 W materials in the different

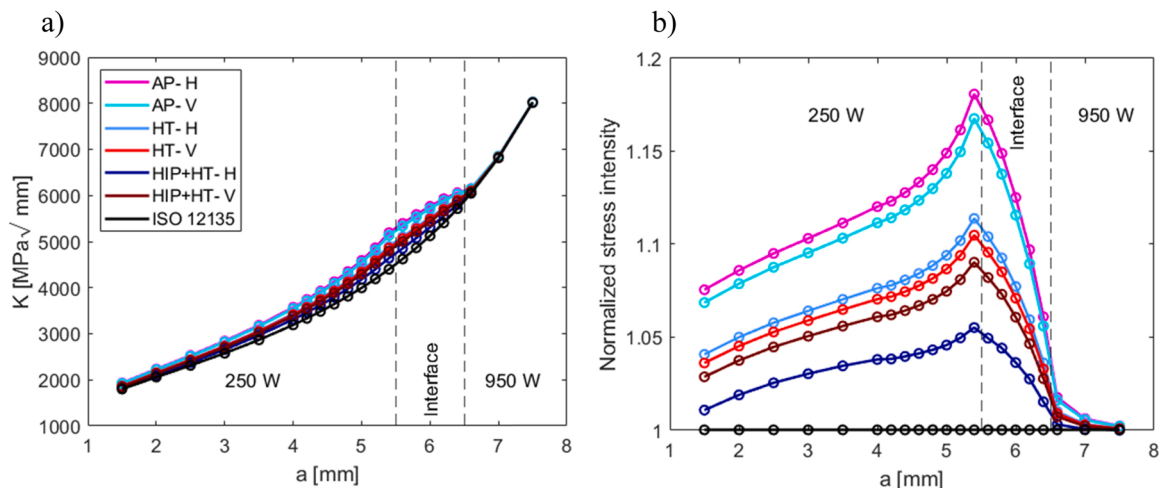


Fig. 16. (a) Stress intensity factor values against the crack length calculated by the FEM model showing the variation of K in the functionally graded specimens for a constant load of 10 kN and (b) the normalized values of the stress intensity against the crack length over the width of the samples. In both plots, the ISO 12135 (ISO, 2016) values are plotted for comparison purposes. The legend given in (a) applies to both figures.

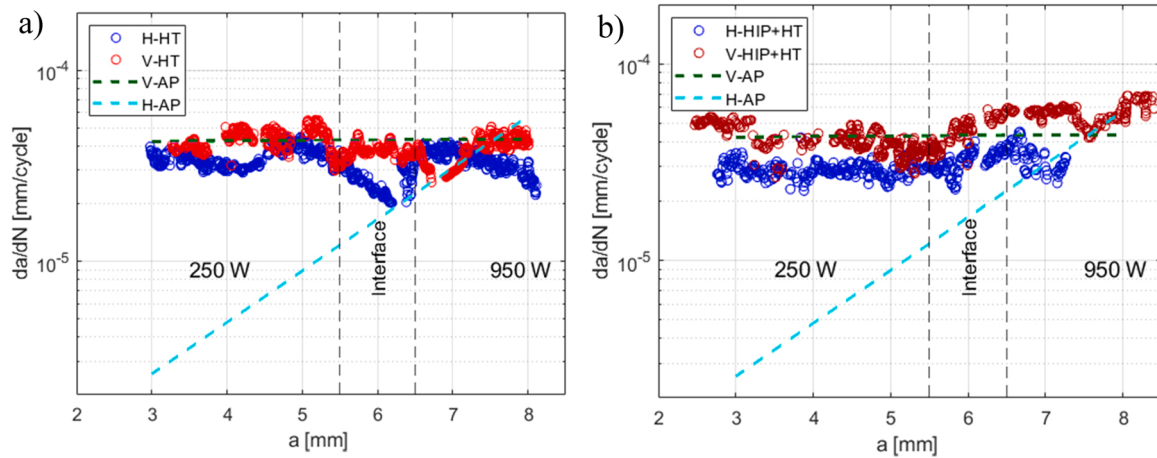


Fig. 17. Fatigue crack growth rate curves of the horizontal and vertical functionally graded samples obtained on the (a) HT and (b) HIP+HT categories in constant ΔK tests. The dashed lines are fits to the data obtained from the tests on the AP materials.

conditions. As it was expected from the GOS plots, the compressive residual stress, which was measured to be -483 ± 74 MPa, decreased to -311 ± 38 MPa after HT and -186 ± 36 MPa after HIP+HT. Similar to the findings in the current study, the level of the compressive RS in the post-processed AM materials was reported to be lower as the heat treatment procedures at $650\text{--}870$ °C can release them (Mishurova et al., 2021).

3.3.3. Fracture surface and crack path

Fracture surface analyses were performed on the functionally graded materials. The SEM micrographs around the interface zones of the AP, HT, and HIP+HT conditions are shown in Fig. 18. It should be noted that the presented micrographs are from the V samples, which showed more defects in the interface area compared with the H specimens. The defects were accumulated in the interface boundaries where the manufacturing parameters changed. As can be seen, the defects are more pronounced on the 250 W side of the interface. In addition, they are visible in the AP

and HT condition materials, while their presence is not significant in the HIP+HT material.

To investigate the type of the defects, higher magnification SEM micrographs, as shown in Fig. 18-d, as well as EDS analyses were performed. It was concluded that the observed defects were unmelted particles which is a common defect in the AM parts of Inconel 718 (Ferreri et al., 2019), Inconel 625 (Hu et al., 2020b), and stainless steel (Molaei et al., 2020). The unmelted or partially melted particles remained in the microstructure since the laser power was not high enough to (fully) melt the larger particles of the powder (Hu et al., 2020a). The unmelted or partially melted particles were still present in the material after the HT process, while their content was significantly reduced after HIP+HT. Also, it should be noted that the materials in AP and HT conditions contain porosity while the HIP+HT post processing reduces the porosity content noticeably, as was reported in different AM alloys such as Inconel 718 (Gribbin et al., 2016a), Ti-6Al-4 V (Cunningham et al., 2016), and stainless steel (Molaei et al., 2020).

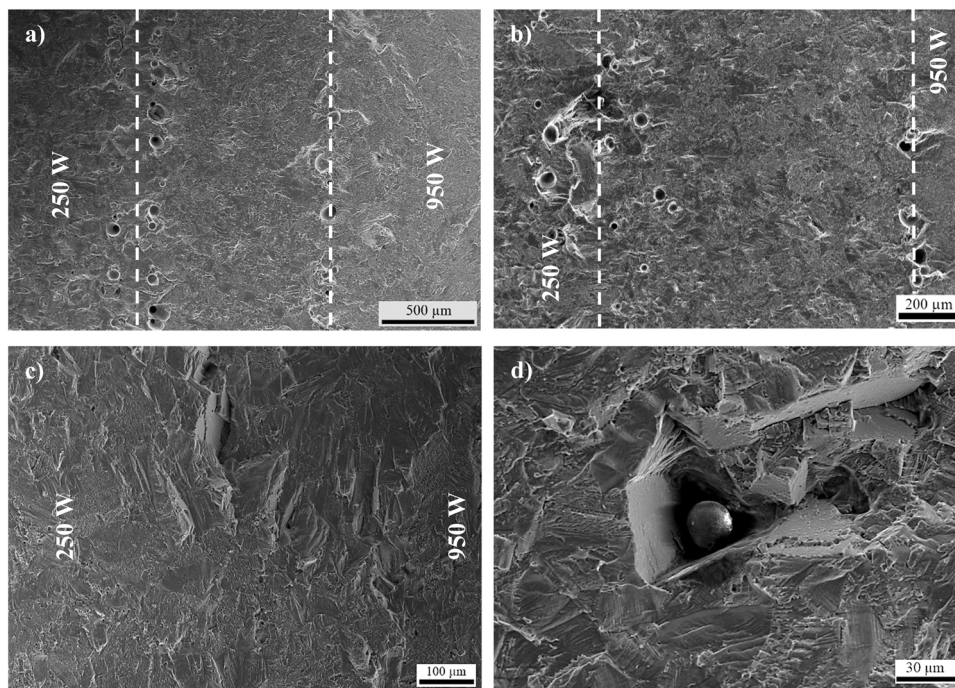


Fig. 18. SEM micrographs of the functionally graded vertical samples around the interface region on the (a) AP, (b) HT, and (c) HIP+HT samples. (d) A high magnification micrograph of an un-melted particle close to the interface zone.

Higher magnification SEM micrographs of the fractured surfaces in the 250 W region of the FG samples in AP, HT, HIP+HT conditions are depicted in Fig. 19. In the fracture surface of the AP material, stair-like features were observed, which can be indications of the local solidification direction. Crack propagation through the epitaxial dendrites revealed those stairs. The stair-like features were also observed in the micrograph of the HT material. In comparison to the AP specimen, however, the stairs seemed to be sharper, featuring lamellae. Those lamellae were accompanied by the secondary microcracks. Such microcracks could be promoted by the strengthening phases to diffuse the stress build-ups. The microcracks are believed to hinder the short crack growth. The formation of the microcracks in this study is consistent with the other research on the AM IN718 superalloy (Pei et al., 2019). The stair-like features were not dominant on the HIP+HT material's fracture surface. Unlike the other two groups, intergranular facets were observed on the micrographs of the HIP+HT samples. The facets originate from the annealing twin boundaries, which were formed after HIP+HT. Extended crystallographic facets develop in the large grains of the HIP+HT microstructure like what was observed in the HIP IN718 in the high cyclic fatigue tests (Gribbin et al., 2019).

Fig. 20 gives the IPF maps of the HT and HIP+HT functionally graded samples as well as the wrought-HT sample in the areas close to the crack. As it was observed for the NG materials shown in Fig. 11, the AM samples kept their directional microstructure in the HT condition while the grains were more equiaxed with random textures in the HIP+HT condition. Clean-ups were not applied to the EBSD data close to the cracks to avoid inducing artefacts. In all maps, as the insert indicates, the crack propagates from right to left. The regions manufactured with different laser powers, and the interface zones are determined in the maps. The characteristics of those zones, i.e., 250 W or 950 W side, remained similar to what was observed in the NG parts. For instance, the grains were finer in the 250 W sides and coarser in the 950 W regions. The texture of the 250 W sides of the HT samples was weaker, while the $\langle 001 \rangle$ preferential direction in the 950 W regions of the HT samples were observed. This behaviour is consistent with the dominant $\langle 001 \rangle$ orientation, which was discussed in the NG EBSD maps. Likewise, the texture of the HIP+HT samples in different zones was similar to their NG counterparts being random in 250 W and 950 W-H, while

moderate in 950 W- V.

The crack paths of the L-PBF samples show the domination of the transgranular fracture mechanism while intergranular fracture happened at some points. This trend was observed for both post-processed conditions and was reported in other research as well (Yu et al., 2021). The fracture mechanism in the wrought material, however, was found to be a combination of intergranular and transgranular fractures. Some deflections were observed on the fracture surfaces of the AM parts. The tortuous crack path on the HT samples' fracture surface can be related to the effect of the melt pools, which have not completely disappeared after the heat treatment (see Fig. 3). In addition, the pinning effect of the rod shape δ precipitates which formed after HT (see Fig. 5), are in favour of crack deflection (Yu et al., 2020). In the HIP+HT samples, the deflections were mostly located close to the annealing twin boundaries. Such deflections can hinder crack propagation (Yu et al., 2021). This is consistent with the lower FCGR observed for the HIP+HT samples in this study.

4. Conclusions

The present work investigated the effects of the L-PBF manufacturing parameters and post-processing procedures on the microstructural and fatigue behaviour of non-graded and functionally graded IN718 produced with different laser parameters and build orientations. The main findings can be summarized as follows:

- 1) The $\langle 001 \rangle$ orientation was found dominant in the non-graded materials while the intensity of the 001 pole was significantly higher in the HT 950 W samples. After HT the grains elongations reduced in the 950 W- H group, while the other materials showed an increase in their grain sizes. HIP+HT changed the grains of the 250 W and 950 W- H materials to equiaxed-like with random textures, while the preferred elongation of the 950 W- V material's grains was preserved.
- 2) The post-heat treatments increased the Vickers hardness of all graded and non-graded materials. The AP graded material showed a direction dependency with a decreasing hardness value pattern along the width for the H samples and near to constant hardness values along

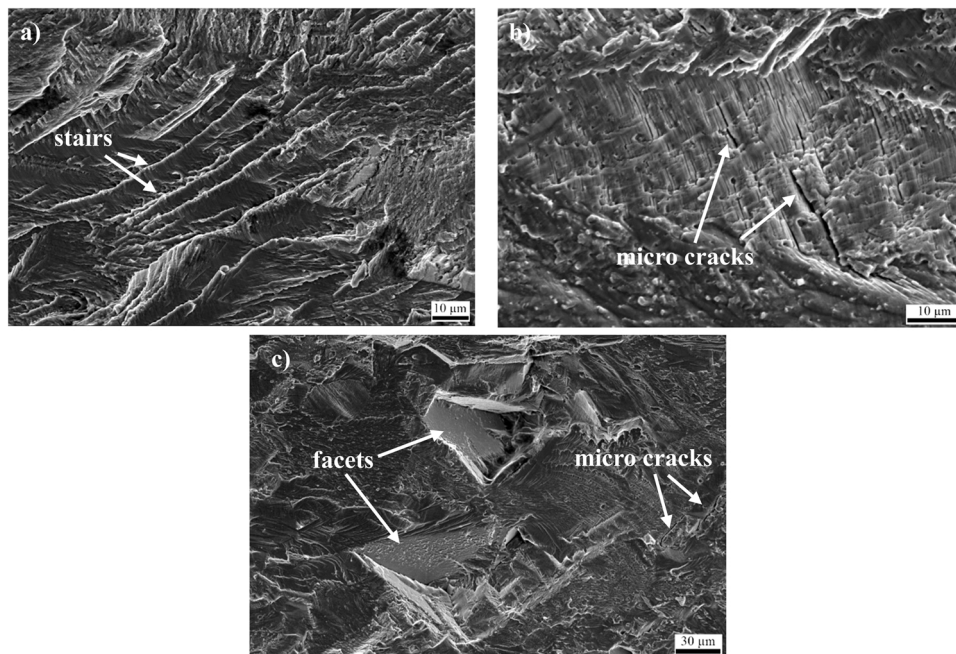


Fig. 19. SEM micrographs of the fractured surfaces in the regions manufactured using 250 W laser power on the (a) AP, (b) HT, and (c) HIP+HT materials. Note that all the images are taken on the H category samples.

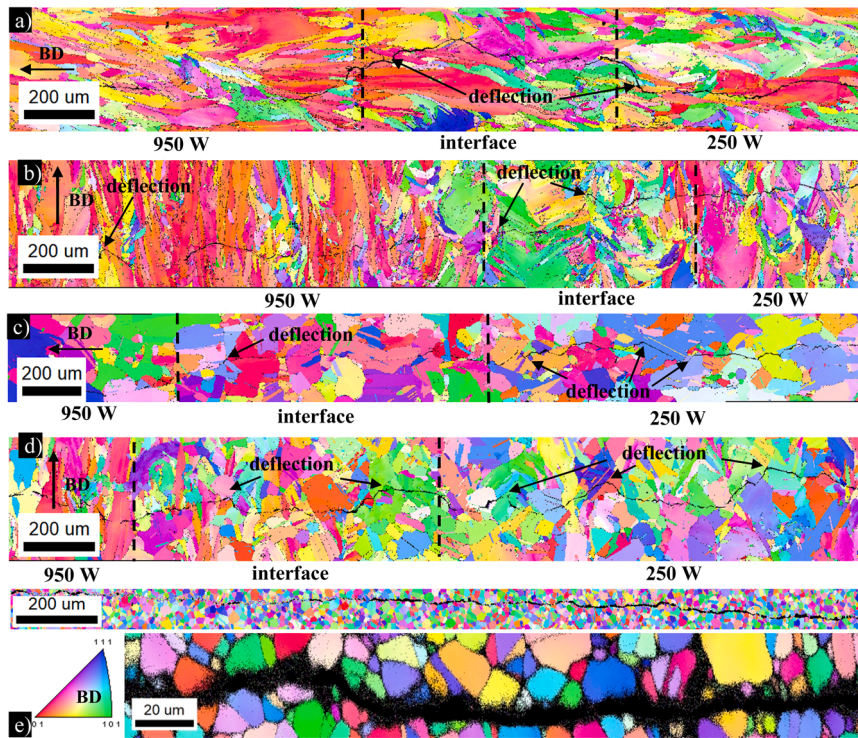


Fig. 20. Inverse pole figure maps of (a) H-HT, (b) V-HT, (c) H-HIP+HT, (d) V-HIP+HT, and (e) wrought-HT samples along the crack path. The IPFs of the L-PBF specimens include the interface region. All samples were tested at a constant ΔK of $22.5 \text{ MPa}\sqrt{\text{m}}$. Note that the micron bars of the L-PBF and wrought IPFs are different. To visualize the crack path of the wrought-HT sample, a higher magnification IPF map is provided in the insert.

the width for the V samples. Although this trend remained similar after post treatment procedures, the slope of the fit in the H samples was reduced which can be related to the higher level of homogeneity in the alloy after the post-treatment.

- 3) At a low stress ratio of $R = 0.1$, in the HT samples the effect of the roughness induced crack closure was found to be higher in the H samples compared with the V specimens, which is related to the elongation of the grains in front of the crack path. After heat treatment, the L-PBF non-graded materials exhibited higher FCGR compared with the wrought-HT samples. However, after HIP+HT, the FCGR improved significantly and reached a lower level than the wrought samples. This behaviour can be a consequence of more isotropic textures and defects reduction.
- 4) At a stress ratio of $R = 0.7$, materials with finer grains had higher threshold stress intensity range which can be caused by the larger number of grain boundaries hindering the crack growth. After post-processing treatments, the ΔK_{th} values in all categories increased which was related to the presence of the strengthening phases and the reduction of defects and porosity.
- 5) The crack path of the L-PBF samples in both post-processed conditions was identified as mostly transgranular, while intergranular fracture was also present. In the wrought-HT material, the fracture was a combination of the intergranular and transgranular fracture. In the L-PBF samples' crack path, deflections were located and mostly happened near the grain boundaries in the HT materials and near the twin boundaries formed during the HIP+HT procedure.

This study comprehensively investigated the effect of the post-processing treatments on anisotropy and improving the fatigue crack growth behaviour of the L-PBF IN718. It was demonstrated that by applying the proper post-processing procedure, the fatigue behaviour can be enhanced to a level even higher than the wrought material. The findings of the current study can be used as a benchmark to establish the most efficient post heat treatment considering the applications of the FG

materials. In addition, although the findings are comprehensive for the room temperature fatigue crack growth behaviours, further investigations at higher temperatures are essential.

CRediT authorship contribution statement

Saeede Ghorbanpour: Methodology, Formal analysis, Investigation, Visualization, Data curation, Validation, Writing – original draft, Writing – review & editing. **Kaustubh Deshmukh:** Methodology, Investigation, Data curation, Visualization. **Saswat Sahu:** Methodology, Investigation, Data curation, Visualization. **Ton Riemsdag:** Methodology, Investigation, Data curation, Visualization. **Elise Reinton:** Methodology, Investigation, Visualization. **Evgenii Borisov:** Methodology, Investigation, Visualization. **Anatolii Popovich:** Methodology, Investigation, Visualization. **Virginia Bertolo:** Methodology, Investigation, Data curation, Visualization. **Quanxin Jiang:** Formal analysis, Investigation, Software. **María Terol Sanchez:** Data curation, Visualization. **Marko Knezevic:** Conceptualization, Writing – original draft, Writing – review & editing. **Vera Popovich:** Methodology, Conceptualization, Funding acquisition, Project administration, Resources, Supervision, Data curation, Writing – original draft, Writing – review & editing.

Declaration of Competing Interest

The authors declare that they have no known competing financial interests or personal relationships that could have appeared to influence the work reported in this paper.

Acknowledgements

We acknowledge the support from the Russian Science Foundation grant (project No. 19-79-30002).

References

- 5663, 19655663, A., 1965. Nickel Alloy, Corrosion and Heat Resistant, Bars, Forgings, and Rings 52.5Ni 19Cr 3.0Mo 5.1Cb 0.90Ti 0.50Al 19Fe, Consumable Electrode or Vacuum Induction Melted 1775°F (968°C) Solution and Precipitation Heat Treated, AMS 5663. SAE International.
- 5664E, A., 1965. Nickel Alloy, Corrosion and Heat Resistant, Bars, Forgings, and Rings, 52.5Ni - 19Cr - 3.0Mo - 5.1Cb - 0.90Ti - 0.50Al - 18Fe, Consumable Electrode or Vacuum Induction Melted, 1950 °F (1066 °C) Solution Heat Treated, Precipitation Hardenable. SAE International.
- Amato, K., Gaytan, S., Murr, L., Martinez, E., Shindo, P., Hernandez, J., Collins, S., Medina, F., 2012. Microstructures and mechanical behavior of Inconel 718 fabricated by selective laser melting. *Acta Mater.* 60, 2229–2239.
- An, J., Wang, L., Liu, Y., Cai, W., Song, X., 2017. The role of δ phase for fatigue crack propagation behavior in a Ni base superalloy at room temperature. *Mater. Sci. Eng. A* 684, 312–317.
- Blochwitz, C., Tirschler, W., 2005. Twin boundaries as crack nucleation sites. *Cryst. Res. Technol.* 40, 32–41.
- Burke, M., Miller, M., 1991. Precipitation in alloy 718: a combined Al₃M and apfim investigation. In: Loria, E.A. (Ed.), *Superalloys 718, 625 and Various Derivatives*. The Minerals, Metals & Materials Society.
- Chlebus, E., Gruber, K., Kuźnicka, B., Kurzac, J., Kurzynowski, T., 2015. Effect of heat treatment on the microstructure and mechanical properties of Inconel 718 processed by selective laser melting. *Mater. Sci. Eng.: A* 639, 647–655.
- Cunningham, R., Narra, S.P., Ozturk, T., Beuth, J., Rollett, A.D., 2016. Evaluating the effect of processing parameters on porosity in electron beam melted Ti-6Al-4V via synchrotron X-ray microtomography. *JOM* 68, 765–771.
- Ding, J., Xue, S., Shang, Z., Li, J., Zhang, Y., Su, R., Niu, T., Wang, H., Zhang, X., 2021. Characterization of precipitation in gradient Inconel 718 superalloy. *Mater. Sci. Eng.: A* 804, 140718.
- E647, A., Standard Test Method for Measurement of Fatigue Crack Growth Rates.
- Feng, K.-y., Liu, P., Li, H.-x., Sun, S.-y., Xu, S.-b., Li, J.-n., 2017. Microstructure and phase transformation on the surface of Inconel 718 alloys fabricated by SLM under 1050°C solid solution + double ageing. *Vacuum* 145, 112–115.
- Ferreri, N.C., Ghorbanpour, S., Bhowmik, S., Lussier, R., Bicknell, J., Patterson, B.M., Knezevic, M., 2019. Effects of build orientation and heat treatment on the evolution of microstructure and mechanical properties of alloy Mar-M-509 fabricated via laser powder bed fusion. *Int. J. Plast.* 121, 116–133.
- Ferreri, N.C., Vogel, S.C., Knezevic, M., 2020. Determining volume fractions of γ , γ' , γ'' , δ , and MC-carbide phases in Inconel 718 as a function of its processing history using an advanced neutron diffraction procedure. *Mater. Sci. Eng.: A* 781, 139228.
- Ghorbanpour, S., Zecevic, M., Kumar, A., Jahedi, M., Bicknell, J., Jorgensen, L., Beyerlein, I.J., Knezevic, M., 2014. A crystal plasticity model incorporating the effects of precipitates in superalloys: Application to tensile, compressive, and cyclic deformation of Inconel 718. *Int. J. Plast.* 99, 162–185.
- Ghorbanpour, S., Sahu, S., Deshmukh, K., Borisov, E., Riemslog, T., Reinton, E., Bertolo, V., Jiang, Q., Popovich, A., Shamshurin, A., Knezevic, M., Popovich, V., 2021. Effect of microstructure induced anisotropy on fatigue behaviour of functionally graded Inconel 718 fabricated by additive manufacturing. *Mater. Charact.* 179, 111350.
- Gribbin, S., Bicknell, J., Jorgensen, L., Tsukrov, I., Knezevic, M., 2016a. Low cycle fatigue behavior of direct metal laser sintered Inconel alloy 718. *Int. J. Fatigue* 93, 156–167.
- Gribbin, S., Bicknell, J., Jorgensen, L., Tsukrov, I., Knezevic, M., 2016b. Low cycle fatigue behavior of direct metal laser sintered Inconel alloy 718. *Int. J. Fatigue* 93, 156–167.
- Gribbin, S., Ghorbanpour, S., Ferreri, N.C., Bicknell, J., Tsukrov, I., Knezevic, M., 2019. Role of grain structure, grain boundaries, crystallographic texture, precipitates, and porosity on fatigue behavior of Inconel 718 at room and elevated temperatures. *Mater. Charact.* 149, 184–197.
- Holland, S., Wang, X., Fang, X.Y., Guo, Y.B., Yan, F., Li, L., 2018. Grain boundary network evolution in Inconel 718 from selective laser melting to heat treatment. *Mater. Sci. Eng.: A* 725, 406–418.
- Hönnige, J., Seow, C.E., Ganguly, S., Xu, X., Cabeza, S., Coules, H., Williams, S., 2021. Study of residual stress and microstructural evolution in as-deposited and inter-pass rolled wire plus arc additively manufactured Inconel 718 alloy after ageing treatment. *Mater. Sci. Eng.: A* 801, 140368.
- Hornbogen, E., Gahr, K.-H.Z., 1976. Microstructure and fatigue crack growth in a γ -Fe-Ni-Al alloy. *Acta Metall.* 24, 581–592.
- Hosseini, E., Popovich, V.A., 2019. A review of mechanical properties of additively manufactured Inconel 718. *Addit. Manuf.* 30, 100877.
- Hu, X., Xue, Z., Ren, T., Jiang, Y., Dong, C., Liu, F., 2020b. On the fatigue crack growth behavior of selective laser melting fabricated Inconel 625: effects of build orientation and stress ratio. *Fatigue Fract. Eng. Mater. Struct.* 43, 771–787.
- Hu, X.-A., Zhao, G.-L., Jiang, Y., Ma, X.-F., Liu, F.-C., Huang, J., Dong, C.-L., 2020a. Experimental Investigation on the LCF behavior affected by manufacturing defects and creep damage of one selective laser melting nickel-based superalloy at 815 °C. *Acta Metall. Sin. (Engl. Lett.)* 33, 514–527.
- Hu, Y., Lin, X., Li, Y., Ou, Y., Gao, X., Zhang, Q., Li, W., Huang, W., 2021. Microstructural evolution and anisotropic mechanical properties of Inconel 625 superalloy fabricated by directed energy deposition. *J. Alloy. Compd.* 870, 159426.
- ISO, 2016. ISO 12135:2016(E). *Met. Mater. — Unif.-. Method Test. Determ. Quasistatic Fract. Toughness* 1–98.
- Iyer, A.H.S., Stiller, K., Leijon, G., Andersson-Östling, H.C.M., Hörnqvist Colliander, M., 2017. Influence of dwell time on fatigue crack propagation in Alloy 718 laser welds. *Mater. Sci. Eng.: A* 704, 440–447.
- Kanagarajah, P., Brenne, F., Niendorf, T., Maier, H.J., 2013. Inconel 939 processed by selective laser melting: effect of microstructure and temperature on the mechanical properties under static and cyclic loading. *Mater. Sci. Eng.: A* 588, 188–195.
- Karami, K., Blok, A., Weber, L., Ahmadi, S.M., Petrov, R., Nikolic, K., Borisov, E.V., Leeftang, S., Ayas, C., Zadpoor, A.A., Mehdipour, M., Reinton, E., Popovich, V.A., 2020. Continuous and pulsed selective laser melting of Ti6Al4V lattice structures: effect of post-processing on microstructural anisotropy and fatigue behaviour. *Addit. Manuf.* 36, 101433.
- King, J.E., 1982. Effects of grain size and microstructure on threshold values and near threshold crack growth in powder-formed Ni-base superalloy. *Metal. Science* 16, 345–355.
- Knezevic, M., Ghorbanpour, S., Ferreri, N.C., Riyad, I.A., Kudzal, A.D., Paramore, J.D., Vogel, S.C., McWilliams, B.A., 2021. Thermo-hydrogen refinement of microstructure to improve mechanical properties of Ti-6Al-4V fabricated via laser powder bed fusion. *Mater. Sci. Eng.: A* 809, 140980.
- Komarasamy, M., Shukla, S., Williams, S., Kandasamy, K., Kelly, S., Mishra, R.S., 2019. Microstructure, fatigue, and impact toughness properties of additively manufactured nickel alloy 718. *Addit. Manuf.* 28, 661–675.
- Konečná, R., Kunz, L., Nicoletto, G., Bača, A., 2016. Long fatigue crack growth in Inconel 718 produced by selective laser melting. *Int. J. Fatigue* 92, 499–506.
- Kouraytem, N., Varga, J., Amin-Ahmadi, B., Mir Mohammad, H., Chanut, R.A., Spear, A. D., Kingstedt, O.T., 2021. A recrystallization heat-treatment to reduce deformation anisotropy of additively manufactured Inconel 718. *Mater. Des.* 198, 109228.
- Kreitzberg, A., Brailovski, V., Turenne, S., 2017. Effect of heat treatment and hot isostatic pressing on the microstructure and mechanical properties of Inconel 625 alloy processed by laser powder bed fusion. *Mater. Sci. Eng.: A* 689, 1–10.
- Li, H.Y., Sun, H.L., Bowen, P., Knott, J.F., 2018. Effects of compressive residual stress on short fatigue crack growth in a nickel-based superalloy. *Int. J. Fatigue* 108, 53–61.
- Liaw, P.K., Logsdon, W.A., 1988. Fatigue Crack. Growth Behav. inconel 706 297 K. 4. 2 K. *Acta Metall.* 36, 1731–1744.
- Liu, F., Lin, X., Yang, G., Song, M., Chen, J., Huang, W., 2011. Microstructure and residual stress of laser rapid formed Inconel 718 nickel-base superalloy. *Opt. Laser Technol.* 43, 208–213.
- Liu, X., Xu, J., Barbero, E., Cao, W.-D., Kennedy, R.L., 2008. Effect of thermal treatment on the fatigue crack propagation behavior of a new Ni-base superalloy. *Mater. Sci. Eng.: A* 474, 30–38.
- Ma, D., Stoica, A.D., Wang, Z., Beese, A.M., 2017. Crystallographic texture in an additively manufactured nickel-base superalloy. *Mater. Sci. Eng.: A* 684, 47–53.
- Maciejewski, K., Jouiad, M., Ghonem, H., 2013. Dislocation/precipitate interactions in IN100 at 650 °C. *Mater. Sci. Eng.: A* 582, 47–54.
- Marchese, G., Parizia, S., Rashidi, M., Saboori, A., Manfredi, D., Ugues, D., Lombardi, M., Hryha, E., Biamino, S., 2020. The role of texturing and microstructure evolution on the tensile behavior of heat-treated Inconel 625 produced via laser powder bed fusion. *Mater. Sci. Eng.: A* 769, 138500.
- Mishurova, T., Artzt, K., Rehmer, B., Haubrich, J., Ávila, L., Schoenstein, F., Serrano-Munoz, I., Requena, G., Bruno, G., 2021. Separation of the impact of residual stress and microstructure on the fatigue performance of LPBF Ti-6Al-4V at elevated temperature. *Int. J. Fatigue* 148, 106239.
- Molaei, R., Fatemi, A., Phan, N., 2020. Multiaxial fatigue of LB-PBF additive manufactured 17-4 PH stainless steel including the effects of surface roughness and HIP treatment and comparisons with the wrought alloy. *Int. J. Fatigue* 137, 105646.
- Mostafa, A., Rubio, Picazo, Brailovski, I., Jahazi, V., Medraj, M., 2017. Structure, texture and phases in 3D printed IN718 alloy subjected to homogenization and HIP treatments. *Metals* 7, 196.
- Moussaoui, K., Rubio, W., Mousseigne, M., Sultan, T., Rezai, F., 2018. Effects of selective laser melting additive manufacturing parameters of Inconel 718 on porosity, microstructure and mechanical properties. *Mater. Sci. Eng.: A* 735, 182–190.
- Newman, J.C., Yamada, Y., 2010. Compression precracking methods to generate near-threshold fatigue-crack-growth-rate data. *Int. J. Fatigue* 32, 879–885.
- Nezhadfar, P.D., Johnson, A.S., Shamsaei, N., 2020. Fatigue behavior and microstructural evolution of additively manufactured Inconel 718 under cyclic loading at elevated temperature. *Int. J. Fatigue* 136, 105598.
- Oblak, J.M., Paulonis, D.F., Duvall, D.S., 1974. Coherency strengthening in Ni base alloys hardened by DO22 γ' precipitates. *Metall. Trans.* 5, 143.
- Paris, P., Erdogan, F., 1963. A critical analysis of crack propagation laws. *J. Basic Eng.* 85, 528–533.
- Park, H.-B., Kim, Y.-H., Lee, B.-W., Rheem, K.-S., 1996. Effect of heat treatment on fatigue crack growth rate of Inconel 690 and Inconel 600. *J. Nucl. Mater.* 231, 204–212.
- Pei, C., Shi, D., Yuan, H., Li, H., 2019. Assessment of mechanical properties and fatigue performance of a selective laser melted nickel-base superalloy Inconel 718. *Mater. Sci. Eng.: A* 759, 278–287.
- Ponnelle, S., Brethes, B., Pineau, A., 2001. Orientational Effects and Influence of Delta Phase on Fatigue Crack Growth Rates in a Forged Disc of INCO718 Superalloy.
- Popovich, V.A., Borisov, E.V., Popovich, A.A., Sufiiarov, V.S., Masaylo, D.V., Alzina, L., 2017a. Functionally graded Inconel 718 processed by additive manufacturing: crystallographic texture, anisotropy of microstructure and mechanical properties. *Mater. Des.* 114, 441–449.
- Popovich, V.A., Borisov, E.V., Popovich, A.A., Sufiiarov, V.S., Masaylo, D.V., Alzina, L., 2017b. Impact of heat treatment on mechanical behaviour of Inconel 718 processed with tailored microstructure by selective laser melting. *Mater. Des.* 131, 12–22.
- SAE AMS 5383, A, 1966. Nickel Alloy, Corrosion and Heat-Resistant, Investment Castings, 52.5Ni - 19Cr - 3.0Mo - 5.1Cb(Nb) - 0.90Ti - 0.60Al - 18Fe, Vacuum Melted Homogenization and Solution Heat Treated. SAE International.

- Sanchez, S., Gaspard, G., Hyde, C.J., Ashcroft, I.A., Ravi, G.A., Clare, A.T., 2021. The creep behaviour of nickel alloy 718 manufactured by laser powder bed fusion. *Mater. Des.*, 109647.
- Segerstark, A., Andersson, J., Svensson, L.-E., Ojo, O., 2018. Microstructural characterization of laser metal powder deposited Alloy 718. *Mater. Charact.* 142, 550–559.
- Smith, D.H., Bicknell, J., Jorgensen, L., Patterson, B.M., Cordes, N.L., Tsukrov, I., Knezevic, M., 2016. Microstructure and mechanical behavior of direct metal laser sintered Inconel alloy 718. *Mater. Charact.* 113, 1–9.
- Sui, S., Chen, J., Fan, E., Yang, H., Lin, X., Huang, W., 2017. The influence of Laves phases on the high-cycle fatigue behavior of laser additive manufactured Inconel 718. *Mater. Sci. Eng.: A* 695, 6–13.
- Tillmann, W., Schaak, C., Nellesen, J., Schaper, M., Aydinöz, M.E., Hoyer, K.P., 2017. Hot isostatic pressing of IN718 components manufactured by selective laser melting. *Addit. Manuf.* 13, 93–102.
- Tochigi, E., Nakamura, A., Shibata, N., Ikuhara, Y., 2018. Dislocation structures in low-angle grain boundaries of α -Al₂O₃. *Crystals* 8, 133.
- Toh, S.F., Rainforth, W.M., 1996. Fatigue of a nickel base superalloy with bimodal grain size. *Mater. Sci. Technol.* 12, 1007–1014.
- Tucho, W.M., Cuvillier, P., Sjolyst-Kverneland, A., Hansen, V., 2017. Microstructure and hardness studies of Inconel 718 manufactured by selective laser melting before and after solution heat treatment. *Mater. Sci. Eng.: A* 689, 220–232.
- Wang, K., Li, M., Luo, J., Li, C., 2011. Effect of the δ phase on the deformation behavior in isothermal compression of superalloy. *Mater. Sci. Eng.: A* 528 (4723–4731), GH4169.
- Wang, X., Chou, K., 2019. The effects of stress relieving heat treatment on the microstructure and residual stress of Inconel 718 fabricated by laser metal powder bed fusion additive manufacturing process. *J. Manuf. Process.* 48, 154–163.
- Wang, Z., Guan, K., Gao, M., Li, X., Chen, X., Zeng, X., 2012. The microstructure and mechanical properties of deposited-IN718 by selective laser melting. *J. Alloy. Compd.* 513, 518–523.
- Yamada, Y., Newman, J.C., 2009. Crack closure under high load-ratio conditions for Inconel-718 near threshold behavior. *Eng. Fract. Mech.* 76, 209–220.
- Yu, X., Lin, X., Liu, F., Hu, Y., Zhang, S., Zhan, Y., Yang, H., Huang, W., 2020. Microstructure and fatigue crack growth behavior of inconel 718 superalloy fabricated via laser directed energy deposition additive manufacturing. *SSRN*.
- Yu, X., Lin, X., Tan, H., Hu, Y., Zhang, S., Liu, F., Yang, H., Huang, W., 2021. Microstructure and fatigue crack growth behavior of Inconel 718 superalloy manufactured by laser directed energy deposition. *Int. J. Fatigue* 143, 106005.
- Zhang, D., Niu, W., Cao, X., Liu, Z., 2015. Effect of standard heat treatment on the microstructure and mechanical properties of selective laser melting manufactured Inconel 718 superalloy. *Mater. Sci. Eng.: A* 644, 32–40.
- Zhang, Y., Li, Z., Nie, P., Wu, Y., 2013. Effect of heat treatment on niobium segregation of laser-cladded IN718 alloy coating. *Metall. Mater. Trans. A* 44, 708–716.
- Zhao, Y., Li, K., Gargani, M., Xiong, W., 2020. A comparative analysis of Inconel 718 made by additive manufacturing and suction casting: microstructure evolution in homogenization. *Addit. Manuf.* 36, 101404.
- Zhou, L., Mehta, A., McWilliams, B., Cho, K., Sohn, Y., 2019. Microstructure, precipitates and mechanical properties of powder bed fused inconel 718 before and after heat treatment. *J. Mater. Sci. Technol.* 35, 1153–1164.